SCIENCE CHINA
Physics, Mechanics & Astronomy

•Invited Review•
Special Topic: Recent Developments and Challenges in Solar Cells

January 2023 Vol. 66 No. 1: 217305
https://doi.org/10.1007/s11433-022-1959-4

Improving intrinsic stability for perovskite/silicon tandem solar cells

Tailai Xu, Yihua Chen[*], and Qi Chen[*]

School of Materials Science and Engineering, Beijing Institute of Technology, Beijing 100081, China

Received April 14, 2022; accepted July 25, 2022; published online November 30, 2022

Monolithic hybrid halide perovskite/crystalline silicon (c-Si) tandem solar cells have demonstrated their great potential to surpass the theoretical efficiency limit of single-junction devices. However, the stability of perovskite sub-cells is inferior to that of the c-Si solar cells that have been commercialized, casting serious doubt about the lifetime of the entire device. During device operation, light and heat are inevitable, which requires special attention. Herein, we review the current understandings of the intrinsic stability of perovskite/c-Si tandems upon light and/or heat aging. First, we summarize the recent understandings regarding light facilitated ion migration, materials decomposition, and phase segregation. In addition, the reverse bias effect on the stability of tandem modules caused by uneven illumination is discussed. Second, this review also summarizes the thermal-induced degradation and mismatch issue, which underlines the system design of perovskite/c-Si tandems. Third, recent strategies to improve the intrinsic stability of perovskite/c-Si tandems under light and/or heat are reviewed, such as composition engineering, crystallinity enhancement, interface modification, material optimization, and device structure modification. At last, we present several potential research directions that have been overlooked, and hope those are helpful for future research on perovskite based tandem solar cells.

perovskite, c-Si, tandem solar cell, light stability, thermal stability, photovoltaic module

PACS number(s): 64.75.+g, 71.20.Nr, 82.50.Hp, 84.60.Jt, 89.30.Cc

Citation: T. Xu, Y. Chen, and Q. Chen, Improving intrinsic stability for perovskite/silicon tandem solar cells, Sci. China-Phys. Mech. Astron. **66**, 217305 (2023), https://doi.org/10.1007/s11433-022-1959-4

1 Introduction

Hybrid halide perovskite solar cells (PSCs) have attracted great attentions in the research community these years. Several impressive advantages, such as bandgap tunability [1-3], high absorptivity [4], low exciton binding energies [4,5], and long carrier diffusion length [6], make PSC a promising candidate for next-generation photovoltaic devices. Up to now, the certified power conversion efficiency (PCE) of PSCs has reached 25.7% [7]. However, for a single-junction solar cell with a fixed bandgap, the transmission of sub-bandgap photons and thermalization loss in absorbing high-energy photons cause major energy loss, as shown in Figure 1(a). PSCs also suffer from radiative recombination and other factors [8] like limited carrier mobility. As the PCEs of both PSCs and c-Si solar cells approach their Shockley-Queisser (SQ) PCE limit [9-14] (Figure 1(b)), perovskite/c-Si tandems (Figure 1(c1)-(c4)) are developed to further minimize the above-mentioned energy loss to improve their PCEs [15].

In two-junction perovskite/c-Si tandem solar cells, c-Si with a bandgap of 1.1 eV is suitable for the bottom absorber [14], which is responsible for the long-wavelength portion of

---

*Corresponding authors (Yihua Chen, email: yhchen@bit.edu.cn; Qi Chen, email: qic@bit.edu.cn)

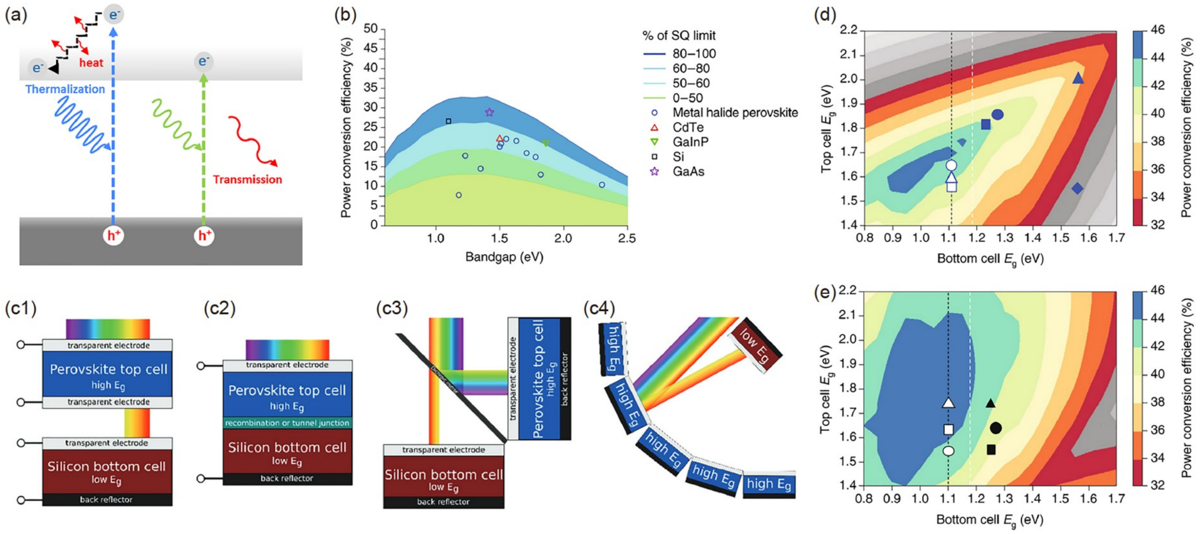

Figure 1 (Color online) (a) Illustration of the intrinsic energy loss of a single junction solar cell, including the thermalization of high energy photon absorption and the transmission of low energy photon. (b) Single junction record PCE with common photovoltaic material in the year 2018. Plotted as a function of bandgap and compared with the SQ limit. The figure is from ref. [14]. Copyright©2018 Springer Nature. Schematics of several perovskite/c-Si tandem architectures: (c1) four-terminal mechanically stacked; (c2) two-terminal monolithically integrated; (c3) four-terminal optical spectral splitting; (c4) four-terminal reflective tandem. The figure is from ref. [15]. Copyright©2018 John Wiley and Sons. The theoretical efficiency limit for (d) two-terminal and (e) four-terminal tandems, calculated with different sub-cell thicknesses, each picked to optimize the performance for each bandgap combination. Grey shading signifies anything below the SQ limit of 32% for a single junction cell with a 1.1 eV bandgap, indicating where there is no efficiency gain in building a tandem device. The dotted white lines mark the lowest bandgap currently accessible to metal halide perovskite semiconductors. The solid symbols indicate bandgap combinations thus far used in making all-perovskite tandems. The black dashed line marks the 1.12 eV bandgap of c-Si, while the open symbols represent the bandgap combinations for the best-achieved two-terminal perovskite/c-Si tandems. The figure is from ref. [14]. Copyright©2018 Springer Nature.

light. And the perovskite with a wide bandgap of 1.6-1.7 eV is achievable for the short-wavelength portion of light [2,3], which pairs with c-Si to yield a theoretical PCE of about 44% [14], as indicated in Figure 1(d) and (e). This combination benefits from mature industry and mass production of c-Si devices, as well as the potential of low-cost perovskite solar cells. According to the record chart of the National Renewable Energy Laboratory (NREL), the PCE of perovskite/c-Si tandem solar cells by Helmholtz Zentrum Berlin [16] have already reached 29.8% [7], surpassing that of any single-junction solar cells. However, for practical applications, a long system lifetime is the basis of cost-efficiency [17]. As shown in Figure 2(a), impressive stability has been obtained in the commercially available c-Si devices [18], where it meets the IEC 61215 standards [19] and guarantees a lifetime of more than 30 years for commercial use [17,20,21]. By contrast, the stability for PSCs is not satisfied yet, which needs more research efforts from the entire community.

Generally, hybrid halide perovskite is vulnerable to water and oxygen [22-25], which can be solved by atmosphere purification and/or device encapsulation [26,27] that blocks the external stressors and provides a chemically inert fabrication/operation environment. However, some other aging stressors, like light and/or heat, in working conditions are inevitable, and have to be treated individually. As illustrated in Figure 2(b), sunlight is absorbed by the perovskite layer, providing energy for carrier generation. But at the same time, illumination could induce the decomposition of perovskite [28] by facilitating ion migration and chemical reaction between the absorber and charge carrier transport layers. Besides, anion segregation occurs easily in perovskite absorbers under sunlight, which generates iodide-rich low-bandgap phases to trap charge carriers. It is also related to excess charge carriers that generated by external bias [29]. Heat is also generated within photovoltaic devices by thermalization, nonradiative recombination, and resistance heating, which would induce perovskite decomposition [30], phase transition [31], and thermal expansion mismatch [32] to result in performance failure.

In this review, we focus on the intrinsic stability of perovskite/c-Si tandem solar cells working in the real world. Specifically, light-induced instabilities, such as ion migration, decomposition, phase segregation, and shading effects are included. We also discuss the generated heat in perovskite/c-Si tandems and its effect on intrinsic stability. We further summarize recent progress to improve device stability, including compositional engineering, crystallinity enhancement, interface modification, material optimization, and device structure modification. Through the in-depth discussions above, we hope to provide a practical and demand-driven view of the working stability of tandem solar cells and contribute to developing robust perovskite/c-Si tandems for commercial applications.

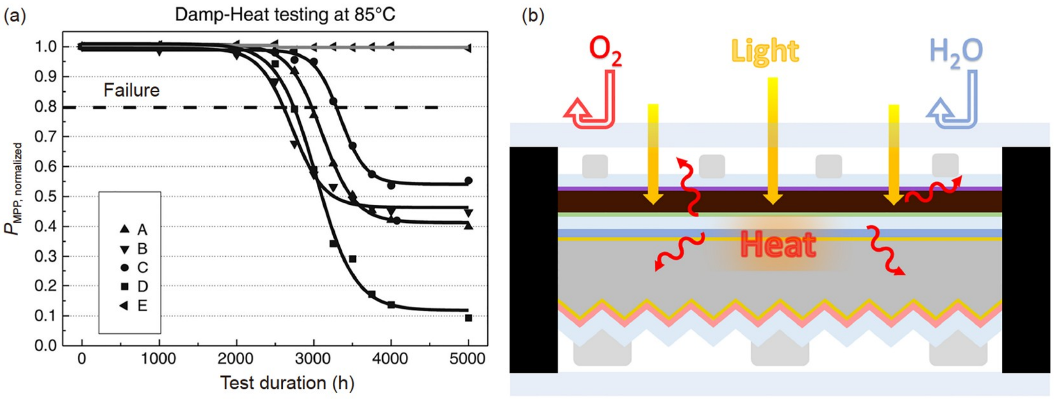

Figure 2 (Color online) (a) Normalized power of the five different silicon photovoltaic module types tested at 85°C and 85% relative humidity as the function of exposure time and fitted degradation curves. The figure is from ref. [18]. Copyright©2017 John Wiley and Sons. (b) Schematic of the effect that encapsulation has on perovskite/c-Si tandem solar cells. Light and resulting heat will not be excluded by encapsulation.

2 Intrinsic stability upon illumination

Illumination is a prerequisite for photovoltaic devices to work. Unfortunately, ion migration often occurs in hybrid halide perovskite under sunlight [33,34], and it leads to mass transport and composition change. Besides, illumination also provides extra energy to promote decomposition and phase segregation [28,29,35-40], which unfavorably increases resistance in the circuits and trapped carriers within the device to deteriorate their stable power outputs. In this section, we discuss the illumination-related ion migration, degradation, phase segregation, as well as other light stability issues originating from uneven illumination and model design for perovskite/c-Si tandem solar cells.

2.1 Illumination-related ion migration

In hybrid halide perovskites, ion migration is observed naturally due to the nature of ionic crystals, which has been widely reported [41]. Electric field-induced ion migration was confirmed by Yang et al. [42] by investigating the electrical properties of $CH_3NH_3PbI_3$ ($MAPbI_3$) with graphite electrodes under the argon atmosphere and in the dark. With alternated current impedance, the measured real part of the complex permittivity is as high as 300 at 1 Hz and 30°C. It can further increase as temperature increases and frequency decreases, which suggests a stoichiometric polarization process. They also set up an all-solid-state electrochemical cell consisting of Pb|$MAPbI_3$|AgI|Ag and applied positive potential on the Pb side. PbI_2 could be detected at the Pb|$MAPbI_3$ interface after charge transference, indicating that I^- can migrate through $MAPbI_3$ material. The influence that illumination has on ionic conductivities was also noticed by them. Another study by Yuan et al. [43] revealed the MA^+ redistribution under an electric field of 1.6 V/μm by using photothermal induced resonance (PTIR). They chose the absorption signal of CH_3 asymmetric deformation as the feature of MA^+, and spotted the redistribution of MA^+ in the lateral Au|$MAPbI_3$|Au device after electrical poling. Furthermore, Pb^{2+} was estimated to have low migration ability due to the high activation energy of 2.31 eV by the calculation of Eames et al. [44]. While the activation energies of MA^+ and I^- vacancies were only 0.84 and 0.58 eV, respectively. Finally, the ion migration pathways in perovskites were concluded by Yuan and Huang [41] and demonstrated in Figure 3(a1)-(a7).

Interestingly, illumination is reported to reduce the activation energies of ion migration. Zhao et al. [34] discovered that activation energy is reduced from 0.39 to 0.074 eV for the $MAPbI_3$ films under illumination by measuring their ionic conductivity concerning the temperature and illumination. The utilized cryogenic galvanostatic measurements carried out by Zhao et al. [33] on Au/$MAPbI_3$/Au devices can be taken as an example, as illustrated in Figure 3(b). In a typical test, a constant current of 20 pA is switched on, then the voltage of the device is measured as a function of time. In the very beginning, both electric field-driven ion migration and carrier drift contribute to the current, and the total conductivity (σ_t) is relatively high (Figure 3(c1)). As migrated ions accumulate at electrodes (Figure 3(c2)), the screening effect emerges and electric field-driven ion migration reaches an equilibrium with ion diffusion, leaving only electron conductivity (σ_e) (Figure 3(c3)). Measured impedance will gradually increase in this process and is finally close to a limitation, as shown in Figure 3(d). As a result, ionic conductivity (σ_{ion}) can be extracted by subtracting σ_e from σ_t. According to the hooping-like transport mechanism, σ_{ion} can be written as:

$$\begin{aligned}\sigma_{\mathrm{ion}}(T)T = ne\mu &= \frac{Z_i e^2 N_A C_{v0} D_0}{k_B V_m}\exp\left(-\frac{G_v}{5k_BT}\right)\exp\left(-\frac{E_a}{k_BT}\right)\\ &= \sigma_0 D_0 \exp\left(-\frac{E_a^{\mathrm{eff}}}{k_BT}\right),\end{aligned} \tag{1}$$

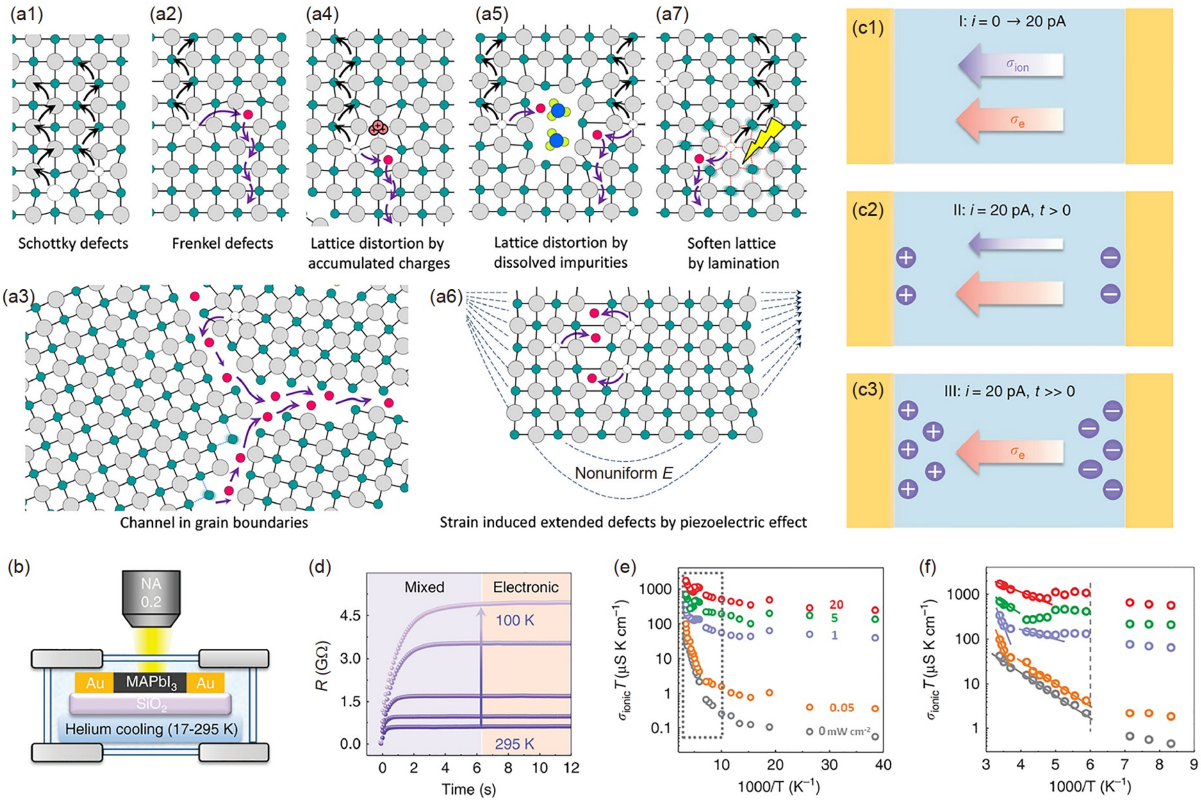

Figure 3 (Color online) Illustration of the ion migration pathways enabled by (a1) Schottky defects, (a2) Frenkel defects, (a3) open space and wrong bonds at grain boundaries, (a4)-(a6) lattice distortions due to accumulated charges (a4), dissolved impurities (a5), and nonuniform strain caused by piezoelectric effect (a6), and (a7) soften lattice caused by the light illumination induced bond weakening. The figure is from ref. [41]. Copyright©2016 American Chemical Society. (b) The apparatus used in the experiments of Zhao et al. with a helium cooling system. The lateral device was prepared on a silica substrate with Au electrodes and mounted on a sample stage with a cooling system. The figure is from ref. [33]. Copyright©2017 Springer Nature. Schematic illustration of (c1) the conductance contributions from both ions and electrons, without any ionic depletion in the perovskite film; (c2) the gradual depletion of mobile ions as they accumulate at the two sides of the film, leading to a reduced ionic contribution to the conductance of the perovskite film; (c3) only electrons contribute to the conductance after the mobile ions in the film have been totally depleted at a sufficiently weak current of 20 pA. The figure is from ref. [33]. Copyright©2017 Springer Nature. (d) Five typical galvanostatic curves (resistance vs. time) recorded at different temperatures under a 20 pA current and 1 mW cm^{-2} illumination. The temperatures from bottom to top are 295, 240, 200, 150, and 100 K, respectively. The figure is from ref. [33]. Copyright©2017 Springer Nature. (e) Ionic conductivity multiplied by temperature, $\sigma_{\rm ion}T$, as a function of 1000/T under various illumination intensities. (f) Zoomed-in view of the data in the dashed box in (e). The dashed line indicates the phase transition temperature. Note that the ionic conductivity under 5 mW cm^{-2} illumination has been multiplied by 2 to distinguish the green dots from the purple dots in the plot. The figure is from ref. [33]. Copyright©2017 Springer Nature.

$$\ln(\sigma_{\rm ion}(T)T) = \ln\sigma_0 + \ln D_0 - \frac{E_{\rm a}^{\rm eff}}{k_{\rm B}} * \frac{1}{T}, \tag{2}$$

where $Z_{\rm i}$ stands for the ionic charge, $N_{\rm A}$ is the Avogadro's constant, $C_{\rm v0}$ stands for the concentration of intrinsic defects, $k_{\rm B}$ is the Boltzmann constant, $V_{\rm m}$ stands for the molar volume of perovskite, D_0 is the diffusion coefficient, $G_{\rm v}$ stands for the formation energy for vacancy defects, and $E_{\rm a}^{\rm eff}$ is the activation energy for ionic diffusion, considering additional energy for mobile point defect formation. The results of measured $\sigma_{\rm ion}$ under different illumination intensities and temperatures are shown in Figure 3(e), while Figure 3(f) is the zoomed-in view of the data in the dashed box. The slope of ln($\sigma_{\rm ion}(T)T$)-1/T fitting is negative and its absolute value is reduced under illumination [33]. According to eq. (2), the activation energy for ionic migration is proportional to the slope of ln($\sigma_{\rm ion}(T)T$)-1/T relation, thus it is reduced as illumination intensity enhances. While the intercept of the fitting line has not been investigated.

The mechanism of illumination reducing the activation energy of ion migration is not been fully revealed yet. But there already have some theories. Based on the research of Ruan et al. [38], photons with lower energy have an inferior ability to facilitate the degradation of perovskite than photons with higher energy. They recorded the process of phase segregation under the same optical intensity but at different wavelengths, and spotted slower phase segregation under 488 nm illumination, compared with that under 407 nm illumination. Thus, they speculated that the excess photon energy provided by 407 nm photons promotes vacancy-mediated iodide migration. More deeply, the excess energy, generated by high-energy photons, is wasted by the thermalization process, the relation between thermalization and reduced energy for activating migrated ions needs more study. Similarly, Shahivandi et al. [39] proposed a theory about the relation between light and ion migration. Ion vacancies are generally neutralized by trapped charge carriers, and immune to electric field force without light. When exposed to light, trapped carriers are excited. Then so-called “ionized” vacancies, the “quasi-ions”, are driven by build-in electric field and unevenly distributed on either side of the perovskite layer, reducing effective electric field intensity by screening effect.

It has been intensively investigated that the influence of ion migration is correlated to interfacial ion accumulation, material degradation, and phase segregation in perovskites. At first, ion migration unavoidably induces interfacial ion accumulation, which results in the hysteresis in current density-voltage (*J*-*V*) measurements and the band bending at the upper and lower interfaces of perovskite. Xiao et al. [45] found that the diode property of the device with poly(3,4-ethylenedioxythiophene):poly(4-styrenesulphonate) (PEDOT:PSS)/perovskite/Au structure is controllable by pre-biasing. Because the work function of PEDOT:PSS and Au are almost the same, the contact property of perovskite/Au and perovskite/PEDOT:PSS interfaces are also similar at the initial state. But after pre-biasing, the mobile ions with different charge accumulated at these two interfaces mentioned above, correspondingly, the work function of perovskite surfaces were changed. As a result, the diode property of the two interfaces differed from each other, and charge carrier selectivity was obtained. Thus under illumination, the device showed current output that depends on the pre-biasing. Calado et al. [46] demonstrated that the mobile ions with a high concentration greater than 10^{17} cm^{-3} and severe nonradiative recombination at interfaces are necessary for the hysteresis phenomenon. Besides, ion migration also participated in the interfacial ion accumulation and performance losses of PSCs under reverse bias [47,48]. According to de Bastiani et al. [49], the daily reversible degradation of perovskite/c-Si-tandem devices during their outdoor test was due to the ion migration and reduced charge extraction in perovskites. The increased hysteresis found in the aged devices strongly supports their opinion. Also, Qian et al. [50] proposed that ion migration could explain the prolonged hotspot effect in perovskite/c-Si tandems after reverse bias. This bias promoted ion migration, and then the short circuit current (I_{SC}) of devices was reduced by ion accumulation and non-radiative recombination at interfaces. To suppress ion migration in perovskite cells, the effective passivation with long alkyl chain organic cations [51], rubidium doping for better crystal quality [52], and strain modulation [53] of wide-bandgap perovskite absorber were investigated in former researches. Based on the proposed mechanics of ion migration, down-shifting materials that limit the energy of incident photons and efficient charge carrier extraction may also be useful to suppress ion migration in the perovskite/c-Si tandem solar cells.

The c-Si sub-cells actually also face the migration of ions, for example, Na^+ from the front glass [54]. However, this ion migration is reported to be driven by an applied electric field and facilitated by ambient temperature. Based on the research of Bai et al. [55], Na^+, H^+, OH^-, Ag^+, $\mathrm{SiO_3}^{2-}$, $\mathrm{AlO_2}^-$, and $\mathrm{CH_3COOH}^-$ are possible by-products in a c-Si solar cell with Al or Ag electrodes, which is encapsulated by soda-lime glass and ethylene-vinyl-acetate (EVA) [55]. But this study only considered the migration of $\mathrm{Na}^+$and its effect on potential induced degradation, instead of the impact of light on ion migration.

2.2 Illumination-related degradation

Composition and crystal structure are crucial for desired material properties. However, it is reported that light often promotes composition change and leads to the decay of device performance. In a perovskite/c-Si tandem solar cell, the composition degradation follows three major pathways, such as matter transportation and interface reactions [28,56-58], or material decomposition [35,38]. Besides, the typical total thickness of perovskite and charge transport layers used in tandems is less than 1 μm. The thin films enable efficient charge transport and minimize parasite absorption. But with large specific surface areas, they are subjected to mass transport or interface reactions. Many researchers have studied the diffusion of Li^+ [56], the distribution of MA^+ in the hole transport layer [58], the erosion of Ag electrode and the destination of Ag^+ [57], as well as the interdiffusion of atoms in different perovskite/hole transport materials (HTM) [59] by employing depth-resolved time-of-flight secondary ion mass spectrometry (TOF-SIMS) or mapping.

Lim et al. [28] investigated the light-induced degradation kinetics of a semi-transparent perovskite solar cell, which resembles an actual sub-cell in a tandem device. The *J*-*V* curves of devices were measured to extract the performance parameters as a function of light soaking time. Clear decays of photovoltaic parameters, like shunting resistance (R_{sh}), open-circuit voltage (V_{OC}), short-circuit current density (J_{SC}), fill factor (FF), and PCE, with regard to the soaking time indicated the degradation process of the device under illumination. While the series resistance (R_{s}) actually increased. Based on the recorded decays, the degradation rate constant ($k_{\mathrm{D},i}$) of photovoltaic parameters (i) in each condition can be extracted. To acquire thermal activation energy ($E_{\mathrm{a},i}$) of degradations, the above analysis was also repeated under different temperatures. Based on the Arrhenius formula, the relation of $k_{\mathrm{D},i}$ and $E_{\mathrm{a},i}$ can be expressed as:

$$\ln\left(k_{\mathrm{D},i}\right) = \ln A - \frac{E_{\mathrm{a},i}}{k_{\mathrm{B}}T}.$$

The authors found a distinct difference between the E_{a} of V_{OC} and other parameters, which suggests two kinds of degradation reactions. They considered that the charge carrier recombination of perovskites was not severely affected by temperature, but the crystallinity of the film was reduced. Voids in Spiro-OMeTAD layer along grain boundaries indicated the ion diffusion and reactions, which were further confirmed by TOF-SIMS. Elnaggar et al. [59] first fabricated the devices that consist of ITO/HTM/Perovskite/[6,6]-phenyl C_{61}-butyric acid methyl ester (PCBM), then exposed them to (35±3) mW cm^{-2} white light soaking. After that, they refreshed the PCBM layer of devices as a comparison, and finally fabricated the top contact to exclude the influence of the electrode. In this experiment, the relation of light-induced degradation and charge transport layers was studied. The authors found that the devices with refreshed PCBM showed improved PCE, which was consistent with a previous study that found MAI escaping the perovskite and occupying cavities in the fullerenes layer [60]. Besides, they performed the same investigation on devices with $Cs_{0.1}$-$FA_{0.9}PbI_3$ perovskite and found a minor but not negligible degradation on $Cs_{0.1}FA_{0.9}PbI_3$/PCBM interface. TOF-SIMS results proved the light-induced reaction between PEDOT: PSS and perovskite. There were obvious inter diffusion of Pb^+, I_2^-, C_2^-, S^-, and the depletion of PbI^+ near the interface, which indicated the formation of Pb-PSS salt and I_2-doped PEDOT. In the case of NiO_x, the formation of PbO and NiI_2 under illumination was verified. These results highlight the importance of material choice in perovskite/c-Si tandems, considering the light-induced matter transportation and chemical reaction between perovskite and charge transport materials. Polymer HTMs without reactive functional groups are prospective.

The perovskite absorber in tandems is designed to absorb photons with relatively high energy. Direct decomposition of the material is reported to happen under illumination, especially under ultraviolet (UV) light. Lee et al. [35] proved that perovskites can degrade under 365 nm UV light in an inert atmosphere. After 210 h of soaking by 7.6 mW cm^{-2} UV light, the PCE of the device was greatly reduced from 12.2% to 1.36%. Interestingly, 1-sun light soaking could partially recover the PCE to 10.4% while resting the device in dark made the performance retrogresses to the degraded state. Further UV soaking put more limit on the recovered PCE, finally, only 35% of the initial PCE could be recovered after 1000 h of UV soaking. The authors considered that UV light would generate charge carriers in the TiO_2 layer and in the perovskite layer near the perovskite/TiO_2 interface. Relatively low ratio of electrons in the perovskite to holes in TiO_2 made holes accumulate at the interface, and such trapped holes would react with I^- ions to generate PbI_2. Finally, the recovery of PCE under 1-sun soaking was due to the defect neutralization by photogenerated carriers. In this respect, the down-shifting material could convert UV photons to the photons with lower energy, and protect the perovskite sub-cells.

Metal electrode erosion and atom/ion diffusion are found to be responsible for device instability too as reported in refs. [57,61]. In perovskite/c-Si tandems, the promising design of top contact is transparent conductive oxides (TCO) combined with metal electrode grids, which gives some distinct advantages in stability. On one hand, the usage of metal electrodes in tandems is far less than that in single junction devices, which not only had cost advantages but also reduced the risk of metal erosion [62,63]. On the other hand, there were some reports that condensed oxide materials could suppress metal electrode erosion [64]. Recently, graphene was confirmed as a good capping layer to prevent metal degradation [65].

2.3 Illumination-related phase segregation

In front of c-Si, the wide-bandgap halide perovskite is employed in perovskite/c-Si tandem devices to harvest sunlight with high energy. For two-terminal tandems, the desirable bandgap for front absorber is 1.65-1.7 eV, while for four-terminal tandems, this range enlarges to 1.6-2.1 eV [14]. To acquire the proper wide-bandgap perovskites, iodide anions (I^-) are partially substituted by bromide anions (Br^-), and the proportion of cesium cation (Cs^+), formamide cation (FA^+), methylamine cation (MA^+), and other possible cations are carefully balanced to control overall properties in the context of PCE and stability.

In hybrid halide perovskites with mixed anions, e.g., $(R)Pb(Br_xI_{1-x})_3$ (R = MA^+, FA^+, Cs^+ or a mixture), it was widely reported [29,36-38,40,66,67] that light induced phase segregation would cause the local composition change, and then impact the local bandgap. In terms of this issue, the photoluminescence (PL) that represents the radiative recombination process is a useful characterization method. Hoke et al. [67] firstly discovered the red-shifted PL peak and sub-bandgap absorption at ~1.7 eV, which indicated that the domains with lower bandgap emerged. The split characteristic peaks in X-ray diffraction (XRD) patterns verified the segregation of halide ions and the formation of iodide-rich minority domains. Later, Duong et al. [29] reported the effect of light and bias on phase segregation of $Rb_{0.05}(Cs_{0.1}MA_{0.15}FA_{0.75})_{0.95}PbI_2Br$ perovskite with a bandgap of 1.73 eV (~720 nm). In a typical device, PL signal of the active area under open circuit condition shifted to ~780 nm, by contrast, that of the inactive area shifted to ~760 nm after 12 h of simulated 1 sunlight exposure. If the cell is held at maximum power point (MPP), only a localized shift of PL signals was observed in the active area, which was due to the localized defects. And negligible phase segregation was observed in the active area under short-circuit condition. These results suggested that remaining charge carriers could facilitate light-induced phase segregation. As for bias, PL signals in the typical device under 1.2 V forward bias shifted, however, PL signals remained intact at 1.0 V reverse bias. Based on the observations above, they proposed the nonequilibrium charge carrier-phonon coupling theory as a possible mechanism.

In addition, Bischak et al. [68] also proposed an electron-phonon coupling model for light-induced phase segregation. They considered that photogenerated electron-hole pairs separate, and deform the surrounding lattice by electron-phonon coupling, as shown in Figure 4(a). Then the charge carrier and deformation field of the surrounding lattice form a polaron. Lattice strain is thus influenced by polarons, and the corresponding calculation shows that halide segregation strongly depends on the strain. From the view of free energies per unit cell in Figure 4(b), photoexcited states show trends of segregation. Then, iodide concentrated clusters naturally generate and disappear in material bulk due to fluctuation. The polaron with charge can be trapped by this low-bandgap cluster, stabilizing it through strain-induced segregation. Finally, as shown in Figure 4(c), the stable phase in the ground state turns to be under the coexistence curve in the photoexcited state, meaning that two different phases can coexist. In this model, the lattice energy is considered, and the interaction between charge carriers and lattice is also explained, while charge carrier energy change is overlooked.

Moreover, Draguta et al. [69] investigated the relationship between phase segregation and the thermodynamics of the entire system, including mixing energy, entropy, and charge carrier energy. They pointed out that the mixing energy (blue line in Figure 4(d)) of $MAPbI_3$ and $MAPbBr_3$ is small enough that mixing entropy can control mixed-phase stability (green line in Figure 4(d)). Compared with the mixed state, the iodide (bromide) rich domain has higher valance band (conduction band) edges. As shown in Figure 4(e), charge carriers tend to be trapped in the iodide-rich domains. This difference of energy band edge together with trapped carriers (especially the holes in iodide-rich regions) contributes to the increase of free energy (red line in Figure 4(d)) in the uniform film under illumination, as compared with the segregated counterpart.

Based on the above-mentioned findings, a comprehensive view of phase segregation in perovskites is gradually established. Phase segregation can be considered a reversible transition between segregated or homogeneous phases, and it is controlled by system free energy. If the free energy of the segregated phase under certain conditions, for example, illuminated, is lower than that of the homogeneous phase, then phase segregation tends to be happen. Between the segregated and homogeneous phases, two distinctions, including halide segregation and charge carrier redistribution, influence the system free energy through changing system energy

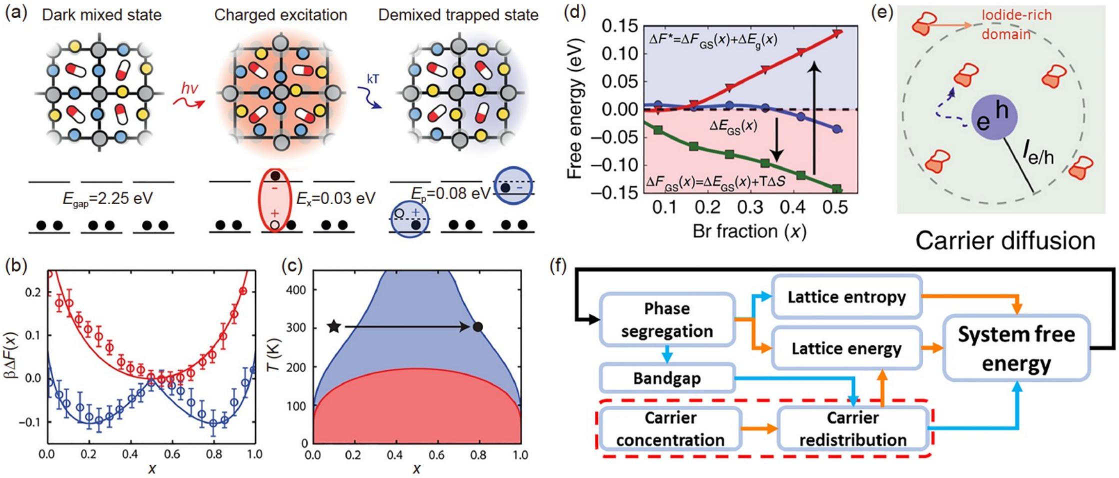

Figure 4 (Color online) (a) Photoinduced polaron trapping and associated energy scales associated with phase separation. Yellow and blue spheres represent I^- and Br^-, respectively. Red and white pill shapes represent MA. Lead atoms are represented by gray circles. The figure is from ref. [68]. Copyright©2017 American Chemical Society. (b) Free energies per unit cell for $MAPb(I_xBr_{1-x})_3$ with varying composition in the ground (red) and photoexcited (blue) states, computed from molecular dynamics simulations (circles) and mean field theory (solid lines). The figure is from ref. [68]. Copyright©2017 American Chemical Society. (c) Mean field theory temperature-composition phase diagram in the ground (red) and photoexcited state (blue) with the path through the phase diagram from the initial state (star) to the demixed state (circle) observed experimentally. Areas beneath the red and blue coexistence curves indicate demixed states. The figure is from ref. [68]. Copyright©2017 American Chemical Society. (d) Estimated free energy of formation as a function of bromide fraction x. The blue line/circles are generalized gradient approximation (GGA)-computed 0 K ground state formation energies, including spin-orbit coupling. The green line/squares are free energies of mixing at 300 K, assuming ideal mixing on the halide sublattice. The red line/inverted triangles represent the free energy difference after single photon absorption. All energies are reported per two formula units. Blue and pink shaded areas indicate positive (phase separation favored) and negative (phase separation disfavored) free energy regions. The figure is from ref. [69]. Copyright©2017 Springer Nature. (e) Schematic of charge carrier diffusion and trapped by the funneling effect of iodide-rich domains. The figure is from ref. [69]. Copyright©2017 Springer Nature. (f) Schematic of system free energy relating processes during phase segregation incident. Orange arrows represent the positive correlation, while blue arrows represent the negative correlation. The red dashed line highlights the process exclusively happens under the light.

or entropy. At first, the concentration of halide ions changes from even distribution to local accumulation. As a result, the system entropy decreases ($\Delta S_{\rm ion}$) due to the composition of the localized I-rich domain differs from the surroundings. Then because of the different radii of iodide and bromide ions, slight lattice structure distortion emerges, leading to the change of the ion binding energy, which is a part of internal energy ($\Delta U_{\rm ion}$). Charge carriers also induce the lattice strain, which can reduce the lattice energy of the segregated phase [68]. Secondly, as compared with the ideal homogeneous condition, it is predicted that charge carriers tend to accumulate in I-rich domains due to their lower bandgap. Concentrated charge carriers have less entropy ($\Delta S_{\rm exciton}$) than that under even distribution condition, but also have less energy ($\Delta U_{\rm exciton}$), because they lost some of the energy during the funneling process [69]. From the homogeneous to segregated phase, the Gibbs free energy change (ΔG) of the system can be calculated as follows:

$$\Delta G = \Delta U_{\rm ion} + \Delta U_{\rm exciton} - T(\Delta S_{\rm ion} + \Delta S_{\rm exciton}).$$

The relationships of the above processes are illustrated in Figure 4(f). Negative ΔG under illumination makes phase segregation favorable in the case of system free energy.

According to the discussion shown in Figure 4(f), some guidelines to achieve superior light stability in perovskites/c-Si tandems are suggested. At first, the mechanisms of phase segregation indicate that it is possible to increase the mixing entropy and binding energy of perovskites, and obtain improved light stability in a point of thermodynamic view by composition engineering [70]. Specifically, the above stable state means that phase segregation would not be thermodynamically favorable even under conventional illumination. Besides, promoting extraction to reduce the concentration of charge carriers in the perovskite absorber could reduce the driving force for phase segregation [29,69]. Also, passivating defects are reported to effectively suppress phase segregation by reducing the route of ion migration [71-73]. Noted that the actual operation of photovoltaic devices could experience the continuous day-night cycle. Therefore, by defect passivation and enhancing charge carrier extraction, the dynamic segregation-recovery equilibrium in perovskites can be reached in day-night cycles, which means that the slight segregation by daytime will fully recover during the night [37]. But the continuous degradation process will introduce more defects in the perovskite cells, gradually limiting daytime performance against phase segregation. Considering the complex interactions among charge carriers, lattice distortion, and bandgap, it still requires more comprehensive investigations on the mechanisms of light-induced phase segregation from different perspectives. Efforts on suppressing phase segregation will be discussed in the later part of this review.

2.4 Realworld illumination and module design

In an actual working condition, the dynamic shading could happen due to the blockage of clouds or objects, which potentially damages the performance of solar modules with series connections. As illustrated in Figure 5(a), the concentration of photogenerated charge carriers in a certain cell in series module reduces, when it is shaded. However, under sunlight, a nearly constant number of charge carriers are collected by the adjacent cell and transferred to the shaded cell by the series connections. In the hole transport layer (HTL) of shaded cells, the injected electrons are more than holes that are collected by the HTL, so electrons accumulate in the HTL and cathode. And similarly, holes accumulate in the electron transport layer (ETL) and anode. Accumulated charges would induce a reverse bias that is applied on the shaded cell, while other cells in the series are slightly forward biased. The maximum reverse bias ($V_{\rm rev,max}$) applied on the cell is determined by the number of other solar cells (N) in this series and the $V_{\rm OC}$ of them, as demonstrated below [74]:

$$V_{\rm rev,max} = V_{\rm OC} \times (N-1).$$

The effect of reverse bias is determined by the magnitude of reverse bias and solar cell structure. Moderate reverse bias has an effect on the hysteresis phenomenon, which was confirmed by Chen et al. [75] and then by Rajagopal et al. [47]. Bowring et al. [76] experimentally characterized the breakdown voltages ($V_{\rm br}$) of PSCs by directly applying reverse bias on them and observing the breakdown phenomenon. The $V_{\rm br}$ results range from -1 to -4 V, which indicated an inferior stability as compared with -15 V $V_{\rm br}$ of the c-Si solar cells. The devices with the architecture of NiO/perovskite/C_{60}/BCP/Ag showed the highest $V_{\rm br}$. The actual degradation occurred in the breakdown cells can be divided into two kinds. (1) Increase in $R_{\rm s}$ and a substantial decrease in $V_{\rm OC}$ can be observed in breakdown cells, which also shows a uniform reverse bias current distribution (see Figure 5(b1)). (2) The locally shunting due to the defects is responsible for the hot spot and consequent permanent damage (see Figure 5(b2)). The first phenomenon is more frequently observed in cells without metal electrodes, which actually resembles the semitransparent perovskite sub-cell utilized in tandems. The reverse bias current is considered the tunneling current near the transport layer/perovskite interface, and will be explained in the later part [76]. And the second phenomenon often happens in cells with metal back electrodes, and the damaged solar cell behaves like a resistor.

Later, Razera et al. [77] studied the effect of reverse bias on devices with the structure of ITO/NiO/perovskite/C_{60}/LiF/SnO_2/ITO/Ag (or other metal). As shown in Figure 5(c1), a reverse bias under -1.1 V caused an abnormal S-shape in the *I-V* curves. And the local shunting happened

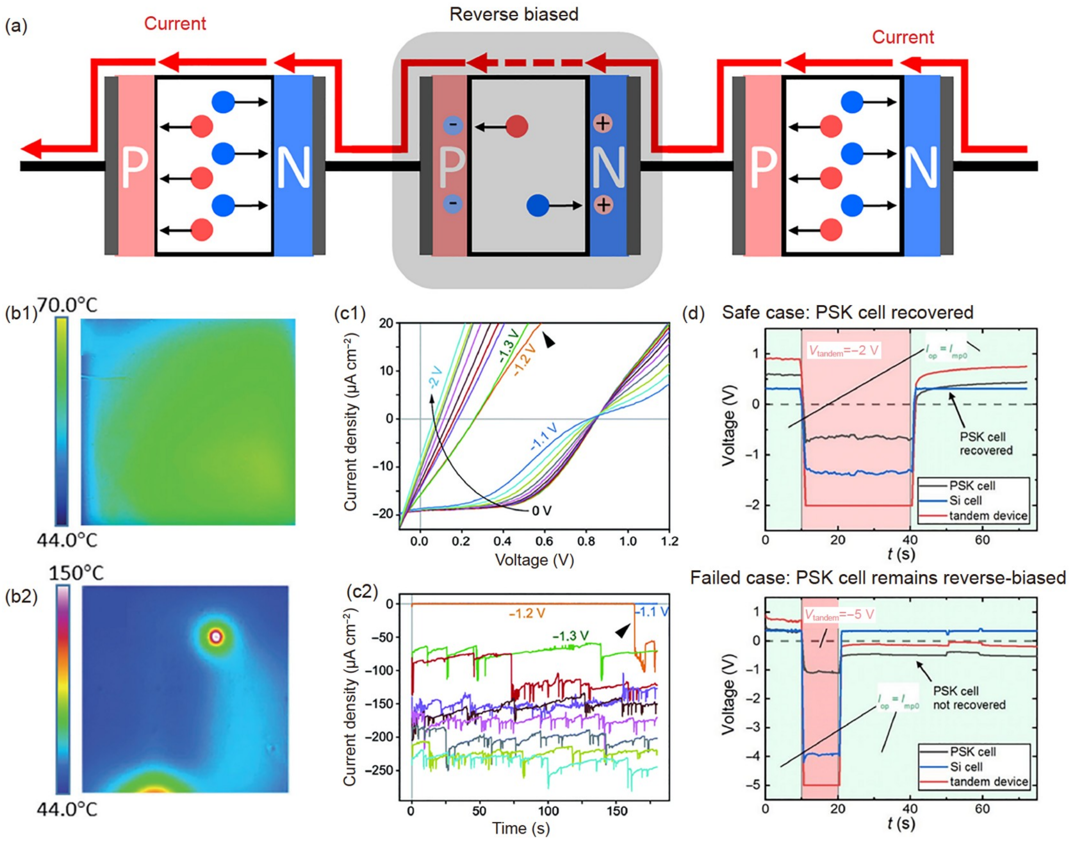

Figure 5 (Color online) (a) Schematic of partial shading caused reverse bias condition. Blue and Red spheres represent holes and electrons. Infrared (IR) images of cells at −5 V showing (b1) uniform breakdown across the whole cell. The slight deviation from uniformity is due to the electrode pattern and the voltage drop across the fairly resistive top ITO electrode (b2) shunting due to local defects. The figure is from ref. [76]. Copyright©2018 John Wiley and Sons. (c1) *I-V* curves taken immediately after biasing the cell at progressively higher (in absolute value) reverse voltages. (c2) Reverse current measured during the 3 min of each reverse biasing step. The figure is from ref. [77]. Copyright©2020 Royal Society of Chemistry. (d) Voltages over time of the perovskite cell, Si cell, and the tandem device during the realistic test in a safe case and a failed case. The figure is from ref. [50]. Copyright©2020 Royal Society of Chemistry.

when the reverse bias is equal to or higher than −1.2 V. The resistor-like behavior of the device in Figure 5(c1) drastically increased the shunting current, as shown in Figure 5(c2), which also supports the emergence of shunting in the device. Then, Qian et al. [50] demonstrated the reverse bias effect on perovskite/c-Si tandem solar cells. In general, perovskite sub-cells could recover after a moderate reverse bias and suffered from a temporary I_{SC} reduction. But when a severe I_{SC} reduction is induced by the huge reverse bias, perovskite sub-cells would remain at reverse biased condition, as shown in Figure 5(d).

Bowring et al. [76] found that the reverse bias current of PSCs first increased and then decayed, which was likely due to an unverified electrochemical reaction. The effect could recover, but became slower as the dark/light cycle under MPP tracking continues. The other two mechanisms of reverse bias that govern the degradation of PSCs are discovered by Razera et al. [77]. One is that iodide ions can be driven into the organic transport layer, which leads to the observed changes of *J-V* curves after reverse bias. This phenomenon is recoverable. Another is that the reverse bias beyond V_{br} can introduce enough charge carriers in the device, which greatly facilitates the phase segregation. The composition of the degraded perovskite under reverse bias showed the iodide and bromide rich sub-layers. It is noted that this effect is irreversible. Recently, the relationship between ion drift-diffusion and electrochemical oxidation is analyzed by Bertoluzzi et al. [48]. Under reverse bias, more positive charges accumulate in the ETL, and vise versa in HTL. The authors considered that if most mobile point defects are halide vacancies, they would drift to HTL under reverse bias, in which the built-in electric field points to HTL. These halide vacancies screened the negative charge in the HTL, so the electric field was more concentrated near the ETL, which narrowed the barrier to the tunneling effect that happened near ETL [62]. As a result, electrons were injected from the valance band of the perovskite to the ETL, leaving more holes in the perovskite. Then accumulated holes reacted with halides, which produced the neutral halogens as recombination centers. If halogens escaped from the perovskite layer, together with other side reactions with adjacent functional layers, the permanent degradation happened.

To solve this issue, Qian et al. [50] predicted that the bypass diodes and high shunt resistance c-Si sub-cells in 2-terminal tandems can protect the perovskite sub-cells. In addition, the suppression of ion migration could also minimize the risk of reverse bias pinning [50]. Further module design aims at preventing the damage of reverse bias will be discussed in the outlook section.

3 Intrinsic stability against thermal aging

Since solar cells are not ideal devices, the generation of heat is inevitable in the light-electricity conversion process. The direct heat radiation from the sun, the thermalization of high energy exciton, and the resistance heat can easily heat solar cells under sunlight to over 65°C. The energy output of photovoltaic modules as a function of temperature is presented by Dupré et al. [78] in Figure 6(a). It is widely reported that the hybrid halide perovskite absorbers are seriously suffered from the heat decomposition, which is attributed to the volatile organic molecules [79,80]. Besides, the high temperature could also facilitate ion migration or diffusion into adjacent layers [61,81]. Finally, sunlight as the heat source is not constant, and it varies during the day, which causes a temperature cycle following the day-night or seasonal cycle during device operation. And the physicochemical and optoelectronic properties of c-Si and perovskite absorbers vary as temperature changes, putting further requirement on current matching and stress-induced structural stability of perovskite/c-Si tandems in temperature cycle [82-85]. In this section, we discuss the causes of device performance decay regarding materials degradation and heat induced mismatch in terms of bandgaps and thermal expansion coefficients (CTEs) within the device.

3.1 Material thermal change

Hybrid perovskite is vulnerable to immense heat. Direct decomposition is often related to organic ions, especially methylammonium that has relatively low molecular weight. Tan et al. [30] have studied the thermal decomposition process of mixed cation perovskite, including $Cs_{0.17}FA_{0.83}Pb(I_{0.83}Br_{0.17})_3$ and $Cs_{0.05}(MA_{0.17}FA_{0.83})_{0.95}Pb(I_{0.83}Br_{0.17})_3$ in air. The decomposition of triple cation perovskites exhibited two decay stages, whereas that of double cation perovskites has only one stage, when the aging temperature is lower than 150°C. This was attributed to the difference of MA^+ and FA^+ cations. Turren-Cruz et al. [86] have reported MA and Br-free perovskites. By using inorganic Rb and Cs ions, they fabricated highly crystalline FACsRb-based perovskites with drastically improved stability. Further removing organic cation ensures the extreme thermal stability of perovskite, for example, $CsPbBr_3$ single crystal can be synthesized by mixing and reacting equimolar amounts of CsBr and $PbBr_2$ in the ampule at 600°C [87]. Beal et al. [3] confirmed a superior thermal stability of $CsPbBrI_2$ than that of $MAPbI_3$ after heating both materials to 180°C. Merely no change of absorbance showed in the UV-vis spectra of $CsPbBrI_2$.

Carrier transport layers are also critical for the thermal stability of PSCs, which can be changed by high temperature. For widely adopted Spiro-OMeTAD, its glass transition temperature (T_G) is ~124°C, enough for the thermal stability requisition of photovoltaic devices [88]. However, the doping by bis(trifluoromethane) sulfonimide lithium salt (Li-TFSI) and 4-tert-butylpyridine (tBP) is commonly used to improve its conductivity [89]. And importantly, the doping can further reduce the T_G of Spiro-OMeTADlayer to about 72°C-91°C [88,90], closing to the operation temperature of solar cells. As shown in Figure 6(b), the crystallization of the Spiro-OMeTAD layer happens inevitably when the device temperature is higher than the T_G. And the crystallized Spiro-OMeTAD can induce pores at the interface, which affects the contact between the perovskite and HTL [31]. These unfavorable change leaves the device more vulnerable to the thermal stress as discussed below. Seo et al. [90] found that substituting Li-TFSI with $Zn\text{-}TFSI_2$ actually raised the T_G of the Spiro-OMeTAD layer by 8°C and improved the T_{80} of the solar cells from ~40 to ~100 h under 1 sun illumination and at 50°C, where the T_{80} is defined as the time when the device retains 80% of its initial PCE. The T_{80} of perovskite devices with the employment of Spiro-OMeTAD material in other researches are still under 100 h when 60°C is applied [88,91].

Similarly to Spiro-OMeTAD, the doping is also conventional when using poly[bis(4-phenyl)(2,4,6-trimethylphenyl) amine] (PTAA), due to its low conductivity [92-94]. The intrinsic PTAA was found to be more stable than the Li^+ doped PTAA, when the devices without encapsulation were aged under 85°C and 85% relative humidity [94]. Even so, Nia et al. [93] demonstrated that their devices with doped PTAA with high molecular weight could retain more than 90% of initial PCE after 1080 h of thermal stress at 85°C. Wang et al. [95] reported that the formation of p-type bulk heterojunction (PCBM doped PTAA) did not affect the stability of the PSCs, but did improve their PCE. Besides, Spalla et al. [96] considered that the perovskites layer is instable under thermal aging, and its decomposition product, HI, was harmful to PTAA layer, which thus reduced the stability of the system.

As for the PEDOT:PSS, it is reported that its acidic functional groups and hygroscopic nature lead to the inferior stability. Lin et al. [97] have investigated the surface modification of glycerol monostearate (GMS) on the PEDOT:PSS. They successfully improved the T_{80} of the device to

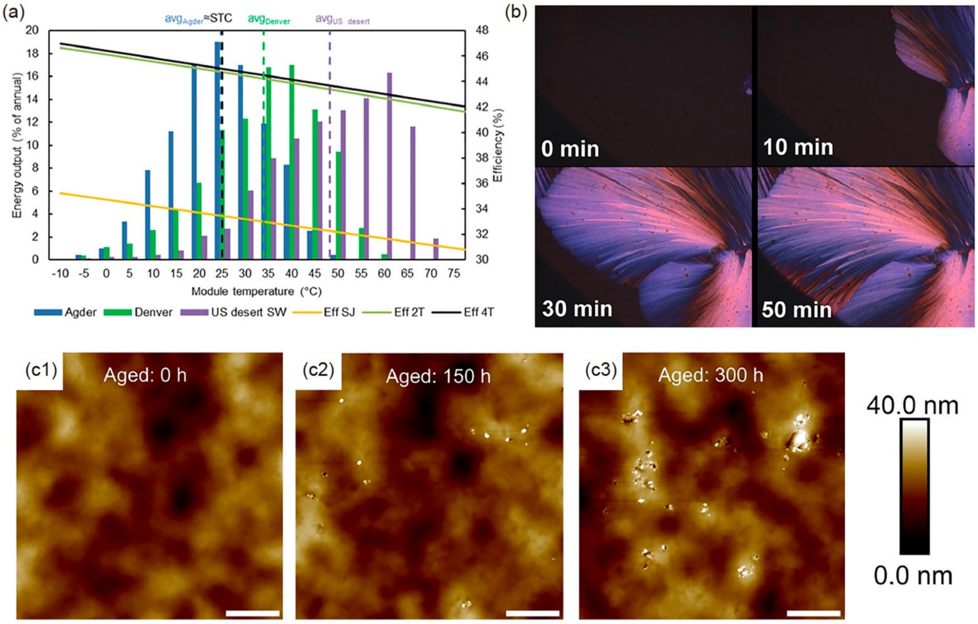

Figure 6 (Color online) (a) The energy output distribution in Agder (Norway), Denver (USA), and a desert in the southwest USA and conversion efficiencies of the single junction and tandem devices as a function of module temperature. The figure is from ref. [78]. Copyright©2018 American Chemical Society. (b) Microscope pictures (dark field crossed polarizers) of the solid-state dye-sensitized solar cell containing Spiro-OMeTAD heated at 100°C. The figure is from ref. [88]. Copyright©2015 American Chemical Society. (c1)-(c3) PCBM films on the perovskite substrates, which were aged under continuous illumination without cooling (surface temperature: 55°C). The scale bar represents 1 μm. The figure is from ref. [114]. Copyright©2021 Science China Press.

~500 h at room temperature in N_2, as compared with ~300 h of the untreated PEDOT:PSS. And the solar cells with PEDOT:PSS are even more vulnerable in air and elevated temperature [98]. Actually PSDOT:PSS is usually found to have the inferior stability compared with other HTLs, such as NiO_x [99,100], PTAA [98] or other materials [101] during the stability characterization of PSCs.

Most inorganic semiconductors are more resistant to heat decomposition. NiO_x is a typical example of inorganic HTL. Zhao et al. [102] discovered that NiO_x based inverted devices almost retained the J_{SC} and V_{OC}, but lost 26% of the initial PCE due to reduced FF after the 80th thermal cycle. Other reports showed that the encapsulated PSCs with ITO/NiO_x/perovskite/LiF/C_{60}/SnO_2/ITO/Ag were capable to pass the IEC 61646 damp heat test and thermal cycling test. Ten devices retained an average 99% of their initial PCE in these tests [26]. Though NiO_x is usually considered to be stable, it is also reported to react with MAI (or HI) at a temperature higher than 100°C [103]. And the reaction of NiO_x with HI is more enthalpy favorable than that of SnO_2 and TiO_2 [104]. Therefore, a proper interface passivation is needed to further improve the stability of PSCs with NiO_x. In addition, another stable HTL is sp^2 hybridized carbon layers, namely graphite with work function near 5.4 eV [105]. Carbon based PSCs have a superior stability and have met IEC61215:2016 standards without apparent degradation [106]. Unfortunately, carbon is not transparent, thus not suitable for perovskite/silicon tandems.

Fullerenes and their derivates are commonly used in PSCs [26,30,59,65] or perovskite/c-Si tandems as ETL [49,85,107,108]. Unfortunately, fullerenes are reported to easily aggregate under thermal stress [109-111]. The monograph of Amabilino [112] reported that C_{60} was highly mobile in many cases, such as migrating between voids formed by the supramolecular structures on Si (111) surface. And the researchers can easily control the migration of C_{60} by varying the tunneling current of scanning tunneling microscopy, which indicates a low energetic barrier to C_{60} motion. Cheacharoen et al. [113] discovered the low fracture energy of the PCBM layer, which suggested that the interaction between these molecules is weak, so the relatively high mobility of the PCBM molecule was predictable. As shown in Figure 6(c1)-(c3), the PCBM layer aggregated under continues illumination and 55°C, which was consistent with previous studies. In order to suppress this effect, Tian et al. [114] synthesized the [6,6]-phenyl-C61-butyric acid benzyl ester (PCBB) molecule, which contained more p-p interactions and thus exhibited superior stability than PCBM films under thermal stress. Still, there are examples that fullerenes based ETLs can withstand 85°C heat aging, and showed the potential of these materials [115,116].

By contrast, the inorganic oxide electron transport materials are much better in thermal stability. There is no doubt in the intrinsic stability of SnO_2 and TiO_2, since their melting points are generally higher than 1500°C. And previous research have proved that SnO_2 and TiO_2 based devices could pass IEC 61646 damp heat test [26], IEC 61646 damp heat test [80,117], even endure worse condition [118]. However, when in contact with perovskite, some light or thermal induced reaction may happen. The photocatalytic activity of TiO_2 has been discussed in the former section. In this regard, SnO_2 has higher bandgap and lower photocatalytic activity as compared with TiO_2, but is also more reactive with HI, which is believed to be the by-product of perovskite under thermal stress. Because the enthalpy of the reaction between HI and SnO_2 (−161 kJ/mol) is lower than that of the equivalent reaction with TiO_2 (−45 kJ/mol) [104].

In c-Si sub-cells, heat does induce the change of material properties. The negative fixed charge density in aluminum oxide (AlO_x) film on the nanostructured silicon was found to decrease after a damp heat test and then limited the passivating effect of AlO_x film [119]. Phua et al. [120] and Karas et al. [121] found that Cu in the finger electrode could diffuse into silicon and cause the nonradiative recombination, though the stability of the cells was still beyond the IEC 61215 standard. Although the internal mechanisms of light- and elevated temperature-induced degradation are not completely revealed, the influence of hydrogen is confirmed [122]. And the moisture-induced degradation is common in c-Si solar cells [123-125]. Therefore, considering the hydrogen-rich nature of organic-inorganic hybrid perovskite and the corrosivity of hydrogen halide, which are even higher than that of water, the synergy between the decomposition of perovskite and the degradation of c-Si sub-cells worth further investigation.

3.2 Bandgaps and CTEs mismatch

The physiochemical and optoelectronic properties of semiconductor materials change as temperature change. When solar cells operate at different temperatures in the day/night, a mismatch happens due to the change of materials properties. As reported by Dupré et al. [78], the actual operating temperature of perovskite/c-Si tandems varies from −5°C to 70°C. And the performance of a perovskite/c-Si solar cell is not essentially stable. Aydin et al. [85] found that the temperature dependent external quantum efficiency (EQE) tests showed a narrowing of the bandgap for c-Si, and a widening of the bandgap for perovskite as the temperature rises, as illustrated in Figure 7(a). And the photovoltaic parameters of perovskite and c-Si sub-cells changed following opposing trends. Thus, the current mismatched and J_{SC} dropped at 75°C in an actual tandem cell. And the match modeling results led them to a conclusion that the optimal bandgap of perovskite fell below 1.68 eV, considering the temperature coefficient of the bandgap. However, Dupré et al. [78] pointed out that due to the Rayleigh scattering of sunlight in the atmosphere, the incident spectrum undergoes a blue shift as the sun rises up, and also as the solar cell heats up. In some cases, the different trend of bandgap shifting for c-Si and perovskite actually conforms with the actual current matching requirements. For example, there is a larger proportion of incoming high energy photons in the noon, which increases the J_{SC} of perovskite sub-cells. Meanwhile, the high energy photons with excess energy can heat perovskite and enlarge its bandgap, so the J_{SC} of c-Si sub-cell is increased simultaneously.

The mismatch of CTE and resulting stress will further cause delamination and fracture in the perovskite/c-Si tandems after the temperature cycle, which is harmful to the stability of devices. As shown in Figure 7(b), clearly that the CTE of perovskite is distinct from that of c-Si. When temperature changes, the expansion of c-Si and perovskite are different. Importantly, the c-Si sub-cell is much thicker than the perovskite sub-cell, so the perovskite sub-cell is compressed at higher temperature or stretched under lower temperature, as illustrated in Figure 7(c). The fracture of resultant devices was observed after the temperature cycle in refs. [84,113]. Such behaviors highlight the importance of the temperature effect and its influence on bandgaps or CTEs mismatch in tandem design. And taking real-world situations into account is beneficial for pursuing the ultimate commercialization of perovskite/c-Si tandems.

4 Improving of intrinsic stability in perovskite/c-Si tandems

There are plenty of reported strategies to improve the intrinsic stability of perovskite/c-Si tandems, especially perovskite sub-cells, which are targeted at different issues, such as ion migration, phase segregation, decomposition or structural damage in perovskite absorber, carrier transport layers, and electrodes. Importantly, the interplay between two sub-cells concerning their degradation behavior should be taken into account to achieve the desirable lifetime of the entire tandem solar cells. The next section will classify and discuss these strategies by presenting actual examples that are worth considering when developing perovskite/c-Si tandems.

4.1 Composition engineering

The intrinsic stability of perovskite is closely bonded to its composition. To improve its resistance to decomposition, many scientists have deeply investigated the composition engineering of perovskite. FACs-based perovskites are widely used in perovskite/c-Si tamed solar cells. As an example, $FAPbI_3$ and $CsPbI_3$ perovskites both have unfavorable tolerance factors, and the α-phase of them are not stable at room temperature. Yi et al. [126] reported that the structural difference between the δ-phase of $FAPbI_3$ and $CsPbI_3$

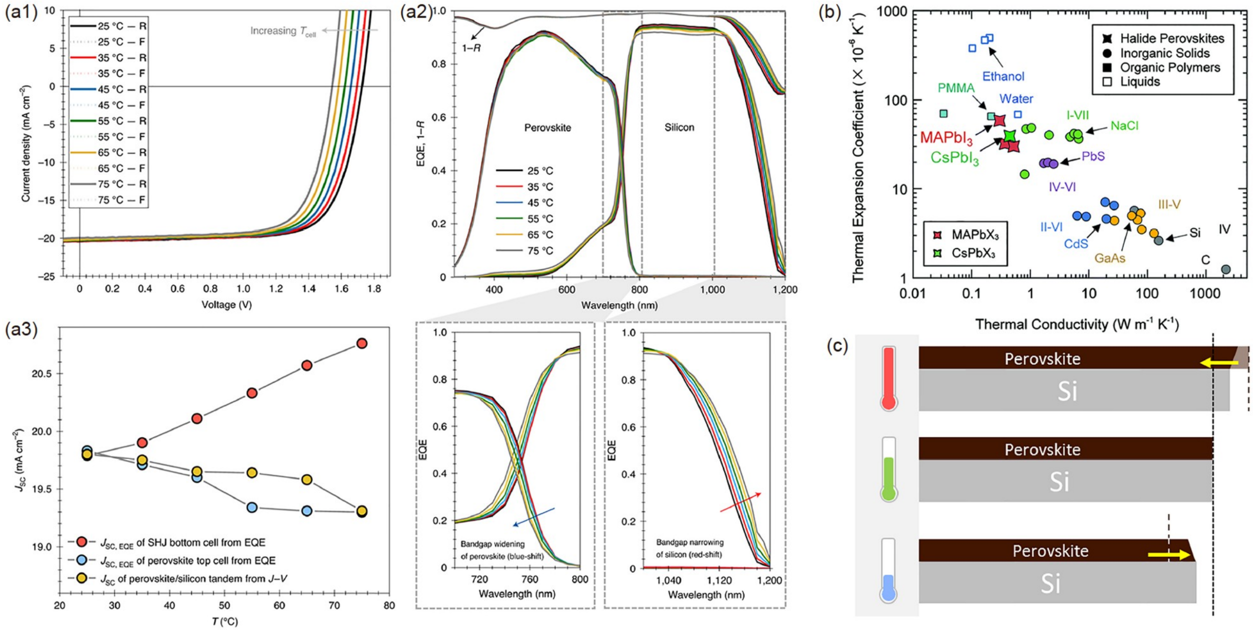

Figure 7 (Color online) (a) Temperature-dependent performance of the perovskite/c-Si tandem solar cells. (a1) Temperature-dependent J-V (R, reverse scan; F, forwards scan) and (a2) EQE and $1-R$ (R is reflectance) characteristics of perovskite/c-Si tandem devices. The bottom of (a2) shows a magnification into the region of the band edge for both sub-cells. (a3) Temperature-dependent change of EQE measured current density ($J_{SC,EQE}$) values for both sub-cells together with the J-V measured current density (J_{SC}) of a tandem solar cell, showing current limiting conditions. The figure is from ref. [85]. Copyright©2020 Springer Nature. (b) CTE vs. thermal conductivity for various materials. The figure is from ref. [32]. Copyright©2020 Royal Society of Chemistry. (c) Schematic of CTE mismatch caused strain. Perovskite material is compressed under high temperature while stretched under low temperature.

made the δ-phase of FACs-mixed cation perovskite energy unfavorable, which explained the improved stability and it was further confirmed by first principal calculations. Bush et al. [36] explored the composition change of $FA_{(1-x)}Cs_xPb(Br_yI_{(1-y)})_3$. PL results proved that Cs should be incorporated with Br to achieve an optimization of the bandgap. Slightly higher content of Cs than Br in perovskite could lead to an improved resistance to halide phase segregation. Wang et al. [127] reported a pure iodide perovskite $Cs_xFA_{1-x-y}DMA_yPbI_3$ ($x > 0.5$; $y < 0.01$) with the assistance of dimethylammonium (DMA) in fabrication, which indicated a wide bandgap of 1.65 eV. This perovskite not only showed a superior thermal stability due to its MA-free nature but also inhibited halide phase segregation from the very beginning.

Apart from the common $FA_{(1-x)}Cs_xPb(Br_yI_{(1-y)})_3$, introducing trace chlorine could also be beneficial to their intrinsic stability. Xu et al. [128] reported a triple halide wide bandgap perovskite. It was found that Br could effectively reduce lattice constant and enable a higher concentration of Cl in the perovskites before the formation of double-phase. As shown in Figure 8(a), the light-induced phase segregation was suppressed in triple-halide perovskites even under 100-sun illumination. The semi-transparent perovskite top cell retained 96% of its initial PCE after 1000 h of MPP tracking in a nitrogen environment. Moreover, introducing other metal ions may also improve the stability of perovskite. Wang et al. [129] confirmed that the K introduced into perovskite precursor could not only get into the lattice as the interstitial ion but also block ion migration pathways. The optimized perovskite film could withstand illumination without the splitting of PL peak, which also presented the reduced defects density and improved storage stability. Duong et al. [52] explored the effect of rubidium (Rb) in perovskite by adding 5% of Rb into $FA_{0.75}(MA_{0.6}Cs_{0.4})_{0.25}PbI_2Br$. This quadruple cation perovskite showed an improved crystallinity and reduced halide phase segregation, which ensured only a 5% reduction of the initial PCE of corresponding devices after 12 h operation.

In addition, by substituting A-site ion with the bulky organic cations, the common three-dimensional (3D) perovskite is split into the cation layer and the lead-halide layer. A so called two-dimensional (2D) or quasi-2D perovskite emerges. Kim et al. [130] introduced two kinds of phenethylammonium (PEA) salts with thiocyanate (SCN) or iodide anions into the perovskite to form a 2D phase. The PEA-based additives with various SCN/(SCN+I) ratios showed different effects on the device performance, and $PEA(I_{0.25}SCN_{0.75})$ devices showed the highest PCE, which retrained 80% of their initial PCE after 1000 h of continues illumination in a nitrogen environment. Quasi-2D perovskite usually possesses great stability, but inferior conductivity due to the spacing organic cation layer. Tsai et al. [131] have overcome this issue by hot-casting, which ensures an out-of-plane alignment of the inorganic lead halide layer. The authors underlined superior stability for this quasi-2D perovskite $((BA)_2(MA)_3Pb_4I_{13})$, where no obvious degradation

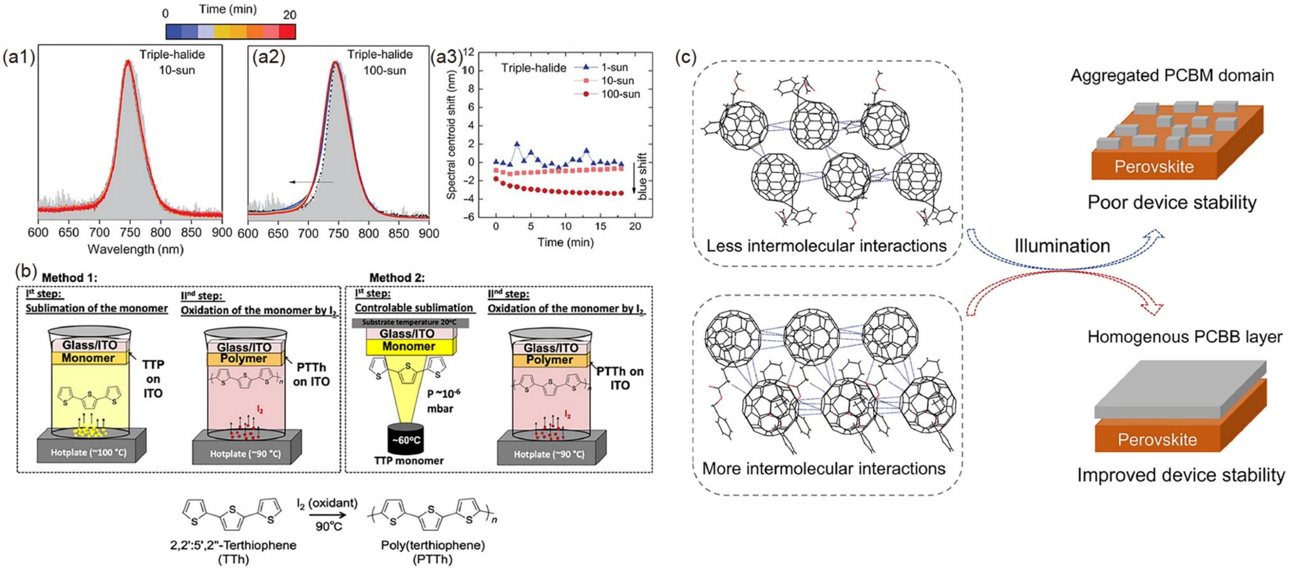

Figure 8 (Color online) (a1), (a2) The PL spectra of 1.67-eV triple-halide perovskites $FA_{0.78}Cs_{0.22}PbI_{2.4}Br_{0.6}$ with $(MAPbCl_3)_{0.03}$ under 10-sun and 100-sun illumination for 20 min, respectively. (a3) The shift of the spectral centroids of triple-halide perovskites over time. The blue shift becomes more obvious under higher injection level. The figure is from ref. [128]. Copyright©2020 The American Association of the Advancement of Science. (b) Film formation processes of PTTh using method 1 in a beaker and method 2 in an evaporation chamber, reaction showing the formation of poly(terthiophene). The figure is from ref. [143]. Copyright©2020 American Chemical Society. (c) Schematic illustration of the influence of fullerene's intermolecular interaction on device stability. The figure is from ref. [114]. Copyright©2021 Science China Press.

was found in the encapsulated device after constant illumination of 2250 h. Notably, it has a bandgap of 1.66 eV, which presents a new way to get a wide-bandgap perovskite absorber while eliminating the possibility of halide phase segregation. The enhanced intrinsic stability of quasi-2D perovskites originated from multiple aspects. First, the light-induced ion migration is found to be suppressed in quasi-2D perovskites, especially across the plane of the inorganic layer [132-134]. And the corresponding degradation processes such as composition change [135] and phase segregation [136] are thus suppressed. This is because the ordered structure of the large cation layer is distinct from the lead halide layer in the terms of lattice structure and chemical environment, so it could hinder the matter transport [134,137]. Besides, the 2D structure was widely employed at grain boundaries in 2D/3D perovskite, and 2D structure was reported to passivate interface defects and block the migration pathways at the same time [138,139].

These examples above indicate that a broad composition space awaits exploration, and halide perovskites can incorporate with a variety of dopants. However, in composition engineering, the overall influence that anion and cation have on the properties of perovskite worth consideration. And at the same time, utilizing the interaction of ions may broaden the range of practical composition tuning.

4.2 Crystallinity enhancement

The better crystallinity of perovskites naturally leads to the less over-all defect states and less grain boundaries. Many corresponding strategies have been reported to improve stability and facilitate charge carrier diffusion of wide-bandgap perovskite. Lau et al. [140] added the half or equal molar ratio of MAI in $CsPbI_3$ precursor. The α-$MAPbI_3$ phase first formed during annealing, and then was substituted by a more thermal stable γ-$CsPbI_3$ phase under higher temperature. This growth process provides a template for γ-$CsPbI_3$ phase, so the better crystallinity and intrinsic stability are achieved. Besides, Li et al. [141] reported that the excess $PbBr_2$ in $CsPbBr_2I$ precursor could form the $Pb(I,Br)_2\cdot$DMSO and $CsPb_2(I,Br)_5$ intermediate phases during annealing. The intermate phases could enhance Ostward ripening, so the corresponding film with a much larger grain size was acquired. And the light-induced phase segregation in the optimized perovskite was also inhibited according to the PL results. Kim et al. [72] introduced a highly polar additive, formamide (CH_3NO), to increase the solubilization of cesium salt in the precursor. The $FA_{0.83}Cs_{0.17}Pb(I_{0.6}Br_{0.4})_3$ perovskite with α-phase directly formed bypassing the yellow phase, and it also showed reduced defects. The light stability of the perovskite absorber and the long-term storage stability of the corresponding device were apparently improved.

4.3 Interface modification

The charge carrier extraction happens on interfaces between perovskite and functional films in perovskite/c-Si tandems, in which some unwanted processes, such as interface recombination or chemical reactions might be suppressed by the interface modification. Zhumagali et al. [142] applied a ruthenium-based metal-organic dye molecule on the interface between NiO_x and perovskite in PSCs. It was found that this interface modification could improve the light and thermal stability of devices, which were attributed to less interface trap assisted degradation, deprotonation of cationic amines, and oxidization of iodide species. Hou et al. [73] reported an anchored self-limiting passivator, 1-butanethiol, to passivate the perovskite absorber on textured c-Si. The vapor process of passivation deals no harm to the perovskite, while the nature of self-limiting for the thiol passivation ensures the precision without the need of careful time control. As surface traps were passivated, carrier trapping and accumulation were reduced, thus, phase segregation in this optimized film was also reduced. This improved the intrinsic stability of perovskite/c-Si tandems.

Introducing additives into perovskites precursor may modify the interfaces, as additives cannot enter the lattice during crystallization and end up between grains. Lin et al. [116] added $[BMP]^+[BF4]^-$ into perovskite precursor, and confirmed this ionic liquid is mainly located as the isolated aggregates between perovskite domains. And small amounts of ionic liquid could penetrate the film and occur at the bottom interface. The authors have found a suppressed release of I_2 in the modified perovskite film under light, which was originated from the passivated or immobilized iodide defects. Instead, Isikgor et al. [107] have reported a molecule (phenformin hydrochloride (PhenHCl)) with both electron-rich and electron-poor moieties, which could passivate defect states and suppress light-induced phase segregation at the same time. And it was also confirmed that the optimized devices exhibited improved PCE and light/thermal stability.

4.4 Material optimization

Due to the chemical activity or other factors, some functional materials in perovskite sub-cell actually induce instability. Apart from the modification, directly replacing them with alternate materials is another solution. Elnaggar et al. [59] made a comparison between the conventional HTLs, such as NiO_x, PTAA, and PEDOT:PSS. They found that the PSCs with PTAA as HTL presents better light stability under continuous illumination, especially after the aged PCBM layer is refreshed. Besides, the micrometer scale silicon pyramids on textured c-Si sub-cell demand conformality of overlying layers. The vapor phase fabrication could meet this demand, but is limited by the molecular weight of raw materials. As shown in Figure 8(b), Suwa et al. [143] have overcome the restriction of polymer evaporation and reported a conformal poly-TTh layer through evaporating terthiophene monomer (TTh) and oxidizing agent iodide. The optimized PSCs demonstrated improved stability as compared with the other evaporable HTL.

For PCBM, this fullerene derivate still suffers from their self-aggregation behavior as discussed above. Changing PCBM with PCBB, which has a more complicated molecule structure and stronger non-covalent intermolecular interactions, could stabilize the ETL under illumination [114]. After the same light-heat aging test, the devices with PCBB as ETL presented a smoother surface, when compared with the distinct aggregation of the PCBM layer in Figure 8(c). Moreover, Neophytou et al. [144] found that the strontium titanate ($SrTiO_3$, ETL) could be synthesized by directly reacting equimolar strontium nitrate ($Sr(NO_3)_2$) and titanium diisopropoxidebis(acetylacetonate) ($C_{16}H_{28}O_6Ti$) at 150°C. It is noted that the $SrTiO_3$ has a higher bandgap, lower fabrication requirement, and less mismatch with perovskites, which makes itself become a promising candidate to conventional TiO_2. The corresponding PSCs with $SrTiO_3$ as ETL showed apparently superior stability during constant illumination.

4.5 Device structure modification

Adding protective layer is a commonly used strategy to stabilize the perovskite sub-cells. The carefully designed protective layer can prevent the ingression of the detrimental atmosphere, the egression of the volatile component, and interface reactions in perovskite sub-cells. Bush et al. [145] reported a protective layer, which consisted of the aluminum doped zinc oxide (AZO) nanoparticle layer and the ITO electrode sputtered on it. They found this layer could effectively prevent the change of PSCs under thermal aging of 100°C, and their XRD patterns could keep the same for 80 min. They considered that the egress of methylammonium iodide was prevented. Besides, the atomic layer deposition (ALD) or chemical vapor deposition (CVD) is a conformal process, which is less likely to form pinholes when the substrate is rough or contaminated by dust. Bush et al. [146] introduced an ALD SnO_2/zinc-tin oxide bilayer as a sputter buffer layer of the ITO electrode into the semi-transparent perovskite sub-cells. They successfully eliminated the pinhole-based degradation in ambient conditions. Their encapsulated devices also passed the IEC 61215 damp heat test. Jeong et al. [65] developed a kind of Cu grid-embedded polyimide film as the substrate and introduced a graphene sheet on it, as shown in Figure 9(a). This graphene sheet effectively suppressed the reaction between perovskite and Cu grid, which was confirmed by TOF-SIMS and aging test. And the results also informed that be aware of metal electrode corrosion when it is not protected. In addition, some other functional layers possess the ability of absorbing UV light. Zheng et al. [147] reported a textured polydimethylsiloxane (PDMS) film with $(Ba,Sr)_2SiO_4{:}Eu^{2+}$, which is a kind of down-shifting material, and its crystal structure is illustrated in Figure 9(b). As the sunlight come in, the UV light is converted to visible light by this topmost

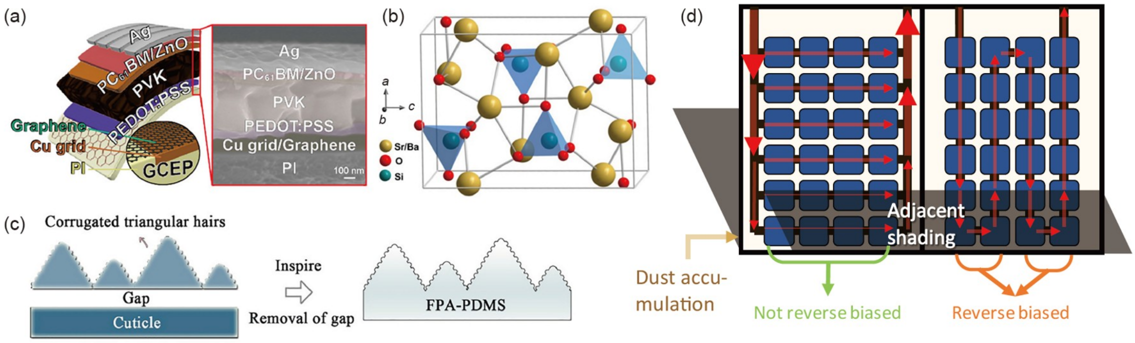

Figure 9 (Color online) (a) Structure of the perovskite device with graphene protection sheet and corresponding cross-sectional scanning electron microscopy image. The figure is from ref. [65]. Copyright©2020 American Chemical Society. (b) Crystal structure of $(Ba,Sr)_2SiO_4$: view of the $(Ba,Sr)_2SiO_4$ along the *b*-axis. The figure is from ref. [147]. Copyright©2019 American Chemical Society. (c) Conceptual description of flexible photonic architectures inspired by silver ants with corrugated triangular hairs and a gap between hairs and cuticle. The figure is from ref. [151]. Copyright©2019 Elsevier. (d) Schematic of series-parallel connection (left) and all series connection (right) under partial shading. As dust and shades of adjacent objects often distribute horizontally, the series-parallel connection can reduce the chance of reverse bias in some of the modules.

layer. And the higher concentration of $(Ba,Sr)_2SiO_4:Eu^{2+}$ in PDMS film provides apparently much better resistances to UV light induced degradation.

Apart from protection, the special structure design is also beneficial to the stability of devices. The poly(methyl methacrylate)/reduced graphene oxide composite buffer layer and Al_2O_3 nanoparticles infiltrated HTL were investigated by Choi et al. [148] and Han et al. [149], respectively. Both reports above claimed that the heat dissipation in their devices is enhanced. Besides, employing the selective-spectral strategy could reduce the heat absorption in PSCs, which means getting rid of a large number of photons that below the bandgap [150]. Enhancing thermal radiation from perovskite modules to the environment is also effective [150]. Moreover, Lin et al. [151] prepared the hierarchically photonic architectures (Figure 9(c)) on PDMS film. This film is transparent to the visible and near infrared light, but shows a better absorption/emittance than bare glass at wavelengths from 8 to 13 μm, which guarantees the direct heat dissipation through atmospheric transmittance window to the universe. Applying these designs could effectively improve the thermal stability of PSCs and perovskite/c-Si tandems.

As for the hotspot problem and reverse bias applied on the cells, they are closely related to photovoltaic module design. Wolf et al. [74] proposed that the series-parallel connection could reduce the number of cells in a string as compared with all series connections. As shown in Figure 9(d), the horizontally connected cells can avoid some shading effects, since debris and the shadow of adjacent module row usually distribute horizontally. The maximum cells number in a string ($N_{\text{string,max}}$) to prevent the breakdown due to reverse bias was calculated according to the cell V_{OC} and V_{br}. And they found that due to much higher V_{br} of the c-Si sub-cells, the $N_{\text{string,max}}$ for monolithic perovskite/c-Si tandems is around 9, which is higher than the $N_{\text{string,max}}$ for PSCs. Considering the uneven distribution of defect states, some cells may have lower V_{br}, so the number of perovskite/c-Si tandems put in parallel with a bypass diode should be lower than the assumption made on ideal cells. Qian et al. [152] considered that four terminal (4T) perovskite/c-Si tandems combined with more bypass diodes and interdigitated back-contact silicon cells could reduce the temperature of the hot spot when the fault operating condition finally happens.

5 Summary and outlook

To commercialize perovskite/c-Si tandem solar cells, it requires the lifetime of perovskite sub-cells being comparable to that of c-Si sub-cells, and the over-all device stability for real-world implementation should be satisfied. Considering current achievements in encapsulation, the effects of environmental oxygen and water on perovskite are primarily solved in principle. By contrast, the intrinsic stability issues in perovskite sub-cells and perovskite/c-Si tandem solar cells, e.g., their resistance against light and/or heat, are not fully addressed and need novel and effective solutions.

In this review, we discussed the intrinsic stability of perovskite/c-Si tandems against light and/or heat aging with a focus on their effects and the underlying mechanisms. Mainly, illumination-induced ion migration, material decomposition, phase segregation, and reverse bias effects are reviewed. And current understandings point out that the first three issues are largely driven by the excess energy of photons and the interaction between charge carriers and perovskite lattice, while the reverse bias is mostly related to the current mismatch between devices in a photovoltaic module. Moreover, we reviewed heat induced degradation in perovskite/c-Si tandems, where the high temperature could induce the change of material properties or trigger the decomposition of vulnerable components. Besides, the temperature cycle in a day or a year could bring mismatch problems, like current density, and thermal expansion in perovskite/c-Si tandems. In the last part, this review focused on the effective strategies to improve the light and/or heat stability of perovskite/c-Si tandems, including composition engineering, crystallinity enhancement, interface modification, material optimization, and device structure modification.

As a commercially available product, the c-Si solar cells have guaranteed 30 years of lifetime, which have surpassed tests according to the IEC standards. For example, the T_{80} of c-Si solar cells have reached 2000 h [18,120] and 4000 h [121] under 85°C and 85% relative humidity damp heat stress. Even with a bias of 1500 V applied between encapsulated solar cells and the module aluminum frame, the T_{80} of the assembled c-Si photovoltaic module was still proved to be ~600 h under damp heat stress [153]. Recent reports show that PSCs can endure damp heat tests as mentioned above, but the light stability of PSCs remains unsatisfactory [93,127,128,130]. Intuitively, the lifetime of perovskite/c-Si tandems is mainly restrained by the perovskite sub cells. As the light stability of perovskite sub-cells keeps going on, which is even comparable to the solar cells based on 2D perovskite and carbon electrode [106], we believe that a lifetime of 8-10 years is a reasonable assumption for perovskite/c-Si tandems in the near future.

At last, our review calls for a deep understanding of stability in some specific aspects. For example, the interactions among photons, charge carriers, and crystal lattice are likely the origin of instability upon illumination. However, it is difficult to decouple simultaneous processes under illumination and materials degradation behavior, which thus hinders the comprehensive understanding of the above interactions. At the same time, the working environments of solar cells are different. An overall consideration to match the two sub cells in perovskite/c-Si tandems by taking these environmental variables into account is just the first step, which requires the actual implementation to prove the effectiveness of the corresponding concepts. To share our limited understandings for further improvement on the intrinsic stability of perovskite/c-Si tandem solar cells, we briefly discuss some challenges that could possibly inspire future research.

(1) Mechanisms of ion migration upon illumination

Light-induced ion migration in perovskites is found to be strongly influenced by the properties of perovskite and the characteristics of incident light. The quantitative analysis of ion migration activation energy was carried out, and the mobile ions in perovskite were confirmed by the experiment. Recent studies have pointed out that illumination intensity and photon energy impact ion migration significantly, but the relation among photon absorption, charge carriers, and ion migration is not fully revealed yet. It is challenging to unveil how photons and charge carriers interact with the crystal lattice of perovskite and ultimately activate ion migration.

Besides, the deeper insight into the mechanisms may provide guidance for future research to enhance the light stability of perovskites and corresponding devices. According to the literatures, two perspectives worth special consideration. The first one is about the photon energy. As higher energy photons are absorbed, the excess energy of generated charge carriers is mostly wasted through thermalization. During this process, the energy is dissipated in the local crystal lattice. Considering ion migration is based on the vibration energy of the lattice, the detailed exploration in the relation of thermalization and ion migration is promising to probe the mechanisms that governs the ion migration upon illumination. The second one is with respect to electron-phonon coupling, wherein charge carriers interact with the surrounding crystal lattice. Bischak et al. [68] reported that the free charges can deform the perovskite lattice. And ion migration actually requires mobile point defects. The formation and movement of point defects are closely related to lattice distortion. In this regard, the reduction of activation energy for ion migration under illumination might be well explained.

(2) Mechanisms of light induced phase segregation

Phase segregation of mix-halide perovskites under light has already been investigated and found to be partially caused by non-equilibrium charge carriers [29]. Unfortunately, current theories mainly focus on the interplay between charge carrier and crystal lattice, while the comprehensive understanding is largely neglected, which may take into account of the system free energy that depends on lattice energy, lattice entropy, charge carrier distribution, and electron-phonon coupling in the phase segregation process. Since these factors add on the complexity of phase segregation in the investigation, the decoupled mechanisms should be clearly illuminated before we obtain the entire map in this field. Therefore, we call for a future study that takes as more factors as possible into account, and then combines the theoretical insights with current achievement in fabricating highly efficient and stable perovskite/c-Si tandems without phase segregation. In addition, if the phase segregation of mix-halide perovskites is found to be thermodynamically inevitable, the dynamic equilibrium between slight segregation at daytime and recovery at night is worth serious consideration.

(3) Module design

Because of the different reverse bias tolerance and heat response in perovskite and c-Si sub-cells, the module design for perovskite/c-Si tandems is urgently required. At first, due to the low breakdown voltage of perovskite sub cells, the cell number of tandems in a series connection has to be reduced, as compared with that in pure c-Si modules [74]. Moreover, the extra bypass diodes and series-parallel connection could reduce the reverse bias albeit of the extra cost. Therefore, its promising to improve the tolerance of PSCs against reverse bias [154,155], especially semitransparent perovskite sub cells in tandems. Meanwhile, the temperature-spectrum-bandgap correlation for perovskite is suggested in the above discussion. For example, the incident light spectrum blue-shift, temperature rising, and bandgap thermal-shift occurs from morning to the noon during a day. Given the variable bandgap, we suggest the full consideration of module design with the data obtained by carrying out field test to maximize power output.

This work was supported by the National Natural Science Foundation of China (Grant Nos. 21975028, 22005035, U21A20172, and 22011540377), Natural Science Funds of the Beijing Municipality (Grant No. JQ19008), China Postdoctoral Science Foundation (Grant No. 2021M700400), and Beijing Institute of Technology Research Fund Program for Young Scholars.

1 C. C. Stoumpos, C. D. Malliakas, and M. G. Kanatzidis, Inorg. Chem. **52**, 9019 (2013).
2 D. P. McMeekin, G. Sadoughi, W. Rehman, G. E. Eperon, M. Saliba, M. T. Hörantner, A. Haghighirad, N. Sakai, L. Korte, B. Rech, M. B. Johnston, L. M. Herz, and H. J. Snaith, Science **351**, 151 (2016).
3 R. E. Beal, D. J. Slotcavage, T. Leijtens, A. R. Bowring, R. A. Belisle, W. H. Nguyen, G. F. Burkhard, E. T. Hoke, and M. D. McGehee, J. Phys. Chem. Lett. **7**, 746 (2016).
4 Q. Lin, A. Armin, R. C. R. Nagiri, P. L. Burn, and P. Meredith, Nat. Photon. **9**, 106 (2015).
5 V. D'Innocenzo, G. Grancini, M. J. P. Alcocer, A. R. S. Kandada, S. D. Stranks, M. M. Lee, G. Lanzani, H. J. Snaith, and A. Petrozza, Nat. Commun. **5**, 3586 (2014).
6 M. B. Johnston, and L. M. Herz, Acc. Chem. Res. **49**, 146 (2016).
7 NREL, *Best Research-Cell Efficiency Chart* (National Renewable Energy Laboratory, Golden, 2022).
8 L. C. Hirst, and N. J. Ekins-Daukes, Prog. Photovolt.-Res. Appl. **19**, 286 (2011).
9 W. Shockley, and H. J. Queisser, J. Appl. Phys. **32**, 510 (1961).
10 M. A. Green, IEEE Trans. Electron. Dev. **31**, 671 (1984).
11 A. Richter, M. Hermle, and S. W. Glunz, IEEE J. Photovolt. **3**, 1184 (2013).
12 W. E. I. Sha, X. Ren, L. Chen, and W. C. H. Choy, Appl. Phys. Lett. **106**, 221104 (2015), arXiv: 1506.09003.
13 I. Almansouri, M. A. Green, and A. Ho-Baillie, J. Mater. Res. **31**, 2197 (2016).
14 T. Leijtens, K. A. Bush, R. Prasanna, and M. D. McGehee, Nat. Energy **3**, 828 (2018).
15 J. Werner, B. Niesen, and C. Ballif, Adv. Mater. Interfaces **5**, 1700731 (2018).
16 A. Al-Ashouri, E. Köhnen, B. Li, A. Magomedov, H. Hempel, P. Caprioglio, J. A. Márquez, A. B. Morales Vilches, E. Kasparavicius, J. A. Smith, N. Phung, D. Menzel, M. Grischek, L. Kegelmann, D. Skroblin, C. Gollwitzer, T. Malinauskas, M. Jošt, G. Matič, B. Rech, R. Schlatmann, M. Topič, L. Korte, A. Abate, B. Stannowski, D. Neher, M. Stolterfoht, T. Unold, V. Getautis, and S. Albrecht, Science **370**, 1300 (2020).
17 X. Tian, S. D. Stranks, and F. You, Sci. Adv. **6**, eabb0055 (2020).
18 M. Koehl, S. Hoffmann, and S. Wiesmeier, Prog. Photovolt.-Res. Appl. **25**, 175 (2017).
19 P. Holzhey, and M. Saliba, J. Mater. Chem. A **6**, 21794 (2018).
20 A. Louwen, W. G. J. H. M. van Sark, R. E. I. Schropp, W. C. Turkenburg, and A. P. C. Faaij, Prog. Photovolt.-Res. Appl. **23**, 1406 (2015).
21 M. M. Lunardi, A. W. Y. Ho-Baillie, J. P. Alvarez-Gaitan, S. Moore, and R. Corkish, Prog. Photovolt.-Res. Appl. **25**, 679 (2017).
22 N. Aristidou, C. Eames, I. Sanchez-Molina, X. Bu, J. Kosco, M. S. Islam, and S. A. Haque, Nat. Commun. **8**, 15218 (2017).
23 J. Yang, Z. Yuan, X. Liu, S. Braun, Y. Li, J. Tang, F. Gao, C. Duan, M. Fahlman, and Q. Bao, ACS Appl. Mater. Interfaces **10**, 16225 (2018).
24 T. Wu, Y. Wang, Z. Dai, D. Cui, T. Wang, X. Meng, E. Bi, X. Yang, and L. Han, Adv. Mater. **31**, 1900605 (2019).
25 T. Bu, J. Li, Q. Lin, D. P. McMeekin, J. Sun, M. Wang, W. Chen, X. Wen, W. Mao, C. R. McNeill, W. Huang, X. L. Zhang, J. Zhong, Y. B. Cheng, U. Bach, and F. Huang, Nano Energy **75**, 104917 (2020).
26 R. Cheacharoen, C. C. Boyd, G. F. Burkhard, T. Leijtens, J. A. Raiford, K. A. Bush, S. F. Bent, and M. D. McGehee, Sustain. Energy Fuels **2**, 2398 (2018).
27 J. Martins, S. Emami, R. Madureira, J. Mendes, D. Ivanou, and A. Mendes, J. Mater. Chem. A **8**, 20037 (2020).
28 J. Lim, M. Kim, H. H. Park, H. Jung, S. Lim, X. Hao, E. Choi, S. Park, M. Lee, Z. Liu, M. A. Green, J. Seo, J. Park, and J. S. Yun, Sol. Energy Mater. Sol. Cells **219**, 110776 (2021).
29 T. Duong, H. K. Mulmudi, Y. L. Wu, X. Fu, H. Shen, J. Peng, N. Wu, H. T. Nguyen, D. Macdonald, M. Lockrey, T. P. White, K. Weber, and K. Catchpole, ACS Appl. Mater. Interfaces **9**, 26859 (2017).
30 W. Tan, A. R. Bowring, A. C. Meng, M. D. McGehee, and P. C. McIntyre, ACS Appl. Mater. Interfaces **10**, 5485 (2018).
31 N. Rolston, B. L. Watson, C. D. Bailie, M. D. McGehee, J. P. Bastos, R. Gehlhaar, J. E. Kim, D. Vak, A. T. Mallajosyula, G. Gupta, A. D. Mohite, and R. H. Dauskardt, Extreme Mech. Lett. **9**, 353 (2016).
32 T. Handa, T. Yamada, M. Nagai, and Y. Kanemitsu, Phys. Chem. Chem. Phys. **22**, 26069 (2020).
33 Y. C. Zhao, W. K. Zhou, X. Zhou, K. H. Liu, D. P. Yu, and Q. Zhao, Light. Sci. Appl. **6**, e16243 (2017).
34 J. Zhao, Y. Deng, H. Wei, X. Zheng, Z. Yu, Y. Shao, J. E. Shield, and J. Huang, Sci. Adv. **3**, o5616 (2017).
35 S. W. Lee, S. Kim, S. Bae, K. Cho, T. Chung, L. E. Mundt, S. Lee, S. Park, H. Park, M. C. Schubert, S. W. Glunz, Y. Ko, Y. Jun, Y. Kang, H. S. Lee, and D. Kim, Sci. Rep. **6**, 38150 (2016).
36 K. A. Bush, K. Frohna, R. Prasanna, R. E. Beal, T. Leijtens, S. A. Swifter, and M. D. McGehee, ACS Energy Lett. **3**, 428 (2018).
37 M. C. Brennan, S. Draguta, P. V. Kamat, and M. Kuno, ACS Energy Lett. **3**, 204 (2018).
38 S. Ruan, M. A. Surmiak, Y. Ruan, D. P. McMeekin, H. Ebendorff-Heidepriem, Y. B. Cheng, J. Lu, and C. R. McNeill, J. Mater. Chem. C **7**, 9326 (2019).
39 H. Shahivandi, M. Vaezzadeh, and M. Saeidi, Sol. Energy Mater. Sol. Cells **208**, 110383 (2020).
40 A. J. Knight, J. B. Patel, H. J. Snaith, M. B. Johnston, and L. M. Herz, Adv. Energy Mater. **10**, 1903488 (2020).
41 Y. Yuan, and J. Huang, Acc. Chem. Res. **49**, 286 (2016).
42 T. Y. Yang, G. Gregori, N. Pellet, M. Grätzel, and J. Maier, Angew. Chem. Int. Ed. **54**, 7905 (2015).
43 Y. Yuan, J. Chae, Y. Shao, Q. Wang, Z. Xiao, A. Centrone, and J. Huang, Adv. Energy Mater. **5**, 1500615 (2015).
44 C. Eames, J. M. Frost, P. R. F. Barnes, B. C. O'Regan, A. Walsh, and M. S. Islam, Nat. Commun. **6**, 7497 (2015).
45 Z. Xiao, Y. Yuan, Y. Shao, Q. Wang, Q. Dong, C. Bi, P. Sharma, A. Gruverman, and J. Huang, Nat. Mater **14**, 193 (2015).
46 P. Calado, A. M. Telford, D. Bryant, X. Li, J. Nelson, B. C. O'Regan, and P. R. F. Barnes, Nat. Commun. **7**, 13831 (2016), arXiv: 1606.00818.
47 A. Rajagopal, S. T. Williams, C. C. Chueh, and A. K. Y. Jen, J. Phys. Chem. Lett. **7**, 995 (2016).
48 L. Bertoluzzi, J. B. Patel, K. A. Bush, C. C. Boyd, R. A. Kerner, B. C. O'Regan, and M. D. McGehee, Adv. Energy Mater. **11**, 2002614 (2021).
49 M. de Bastiani, E. van Kerschaver, Q. Jeangros, A. Ur Rehman, E. Aydin, F. H. Isikgor, A. J. Mirabelli, M. Babics, J. Liu, S. Zhumagali, E. Ugur, G. T. Harrison, T. G. Allen, B. Chen, Y. Hou, S. Shikin, E. H. Sargent, C. Ballif, M. Salvador, and S. de Wolf, ACS Energy Lett.

6, 2944 (2021).
50 J. Qian, M. Ernst, D. Walter, M. A. Mahmud, P. Hacke, K. Weber, M. Al-Jassim, and A. Blakers, Sustain. Energy Fuels **4**, 4067 (2020).
51 T. Duong, H. Pham, Y. Yin, J. Peng, M. A. Mahmud, Y. L. Wu, H. Shen, J. Zheng, T. Tran-Phu, T. Lu, L. Li, A. Kumar, G. G. Andersson, A. Ho-Baillie, Y. Liu, T. White, K. Weber, and K. Catchpole, J. Mater. Chem. A **9**, 18454 (2021).
52 T. Duong, Y. L. Wu, H. Shen, J. Peng, X. Fu, D. Jacobs, E. C. Wang, T. C. Kho, K. C. Fong, M. Stocks, E. Franklin, A. Blakers, N. Zin, K. McIntosh, W. Li, Y. B. Cheng, T. P. White, K. Weber, and K. Catchpole, Adv. Energy Mater. **7**, 1700228 (2017).
53 L. Wang, Q. Song, F. Pei, Y. Chen, J. Dou, H. Wang, C. Shi, X. Zhang, R. Fan, W. Zhou, Z. Qiu, J. Kang, X. Wang, A. Lambertz, M. Sun, X. Niu, Y. Ma, C. Zhu, H. Zhou, J. Hong, Y. Bai, W. Duan, K. Ding, and Q. Chen, Adv. Mater. **34**, 2201315 (2022).
54 J. Šlamberger, M. Schwark, B. B. van Aken, and P. Virtič, Energy **161**, 266 (2018).
55 Q. Bai, H. Yang, C. Nan, H. Wang, and Z. Chen, Sol. Energy **225**, 718 (2021).
56 Z. Li, C. Xiao, Y. Yang, S. P. Harvey, D. H. Kim, J. A. Christians, M. Yang, P. Schulz, S. U. Nanayakkara, C. S. Jiang, J. M. Luther, J. J. Berry, M. C. Beard, M. M. Al-Jassim, and K. Zhu, Energy Environ. Sci. **10**, 1234 (2017).
57 T. Zhang, X. Meng, Y. Bai, S. Xiao, C. Hu, Y. Yang, H. Chen, and S. Yang, J. Mater. Chem. A **5**, 1103 (2017).
58 Y. Zhao, W. Zhou, H. Tan, R. Fu, Q. Li, F. Lin, D. Yu, G. Walters, E. H. Sargent, and Q. Zhao, J. Phys. Chem. C **121**, 14517 (2017).
59 M. Elnaggar, A. G. Boldyreva, M. Elshobaki, S. A. Tsarev, Y. S. Fedotov, O. R. Yamilova, S. I. Bredikhin, K. J. Stevenson, S. M. Aldoshin, and P. A. Troshin, Sol. RRL **4**, 2000191 (2020).
60 A. F. Akbulatov, L. A. Frolova, M. P. Griffin, I. R. Gearba, A. Dolocan, D. A. V. Bout, S. Tsarev, E. A. Katz, A. F. Shestakov, K. J. Stevenson, and P. A. Troshin, Adv. Energy Mater. **7**, 1700476 (2017).
61 K. Domanski, J. P. Correa-Baena, N. Mine, M. K. Nazeeruddin, A. Abate, M. Saliba, W. Tress, A. Hagfeldt, and M. Grätzel, ACS Nano **10**, 6306 (2016).
62 B. A. Kamino, B. Paviet-Salomon, S. J. Moon, N. Badel, J. Levrat, G. Christmann, A. Walter, A. Faes, L. Ding, J. J. Diaz Leon, A. Paracchino, M. Despeisse, C. Ballif, and S. Nicolay, ACS Appl. Energy Mater. **2**, 3815 (2019).
63 Z. Li, H. Li, L. Chen, J. Huang, W. Wang, H. Wang, J. Li, B. Fan, Q. Xu, and W. Song, Sol. Energy **206**, 294 (2020).
64 Z. Wei, B. Smith, F. de Rossi, J. R. Searle, D. A. Worsley, and T. M. Watson, J. Mater. Chem. C **7**, 10981 (2019).
65 G. Jeong, D. Koo, J. Seo, S. Jung, Y. Choi, J. Lee, and H. Park, Nano Lett. **20**, 3718 (2020).
66 A. J. Barker, A. Sadhanala, F. Deschler, M. Gandini, S. P. Senanayak, P. M. Pearce, E. Mosconi, A. J. Pearson, Y. Wu, A. R. Srimath Kandada, T. Leijtens, F. de Angelis, S. E. Dutton, A. Petrozza, and R. H. Friend, ACS Energy Lett. **2**, 1416 (2017).
67 E. T. Hoke, D. J. Slotcavage, E. R. Dohner, A. R. Bowring, H. I. Karunadasa, and M. D. McGehee, Chem. Sci. **6**, 613 (2015).
68 C. G. Bischak, C. L. Hetherington, H. Wu, S. Aloni, D. F. Ogletree, D. T. Limmer, and N. S. Ginsberg, Nano Lett. **17**, 1028 (2017), arXiv: 1606.07366.
69 S. Draguta, O. Sharia, S. J. Yoon, M. C. Brennan, Y. V. Morozov, J. S. Manser, P. V. Kamat, W. F. Schneider, and M. Kuno, Nat. Commun. **8**, 200 (2017).
70 I. M. Pavlovetc, A. Ruth, I. Gushchina, L. Ngo, S. Zhang, Z. Zhang, and M. Kuno, ACS Energy Lett. **6**, 2064 (2021).
71 A. Ruth, M. C. Brennan, S. Draguta, Y. V. Morozov, M. Zhukovskyi, B. Janko, P. Zapol, and M. Kuno, ACS Energy Lett. **3**, 2321 (2018).
72 J. Kim, M. I. Saidaminov, H. Tan, Y. Zhao, Y. Kim, J. Choi, J. W. Jo, J. Fan, R. Quintero-Bermudez, Z. Yang, L. N. Quan, M. Wei, O. Voznyy, and E. H. Sargent, Adv. Mater. **30**, 1706275 (2018).
73 Y. Hou, E. Aydin, M. de Bastiani, C. Xiao, F. H. Isikgor, D. J. Xue, B. Chen, H. Chen, B. Bahrami, A. H. Chowdhury, A. Johnston, S. W. Baek, Z. Huang, M. Wei, Y. Dong, J. Troughton, R. Jalmood, A. J. Mirabelli, T. G. Allen, E. van Kerschaver, M. I. Saidaminov, D. Baran, Q. Qiao, K. Zhu, S. de Wolf, and E. H. Sargent, Science **367**, 1135 (2020).
74 E. J. Wolf, I. E. Gould, L. B. Bliss, J. J. Berry, and M. D. McGehee, Sol. RRL **6**, 2100239 (2022).
75 H. W. Chen, N. Sakai, M. Ikegami, and T. Miyasaka, J. Phys. Chem. Lett. **6**, 164 (2015).
76 A. R. Bowring, L. Bertoluzzi, B. C. O'Regan, and M. D. McGehee, Adv. Energy Mater. **8**, 1702365 (2018).
77 R. A. Z. Razera, D. A. Jacobs, F. Fu, P. Fiala, M. Dussouillez, F. Sahli, T. C. J. Yang, L. Ding, A. Walter, A. F. Feil, H. I. Boudinov, S. Nicolay, C. Ballif, and Q. Jeangros, J. Mater. Chem. A **8**, 242 (2020).
78 O. Dupré, B. Niesen, S. de Wolf, and C. Ballif, J. Phys. Chem. Lett. **9**, 446 (2018).
79 H. Gaonkar, J. Zhu, R. Kottokkaran, B. Bhageri, M. Noack, and V. Dalal, ACS Appl. Energy Mater. **3**, 3497 (2020).
80 L. Shi, T. L. Young, J. Kim, Y. Sheng, L. Wang, Y. Chen, Z. Feng, M. J. Keevers, X. Hao, P. J. Verlinden, M. A. Green, and A. W. Y. Ho-Baillie, ACS Appl. Mater. Interfaces **9**, 25073 (2017).
81 S. Y. Jeong, H. S. Kim, and N. G. Park, ACS Appl. Mater. Interfaces **14**, 34220 (2022).
82 W. W. Zhang, H. Yu, S. Y. Lei, and Q. A. Huang, J. Micromech. Microeng. **22**, 085007 (2012).
83 Y. Kawamura, H. Mashiyama, and K. Hasebe, J. Phys. Soc. Jpn. **71**, 1694 (2002).
84 C. Ramirez, S. K. Yadavalli, H. F. Garces, Y. Zhou, and N. P. Padture, Scripta Mater. **150**, 36 (2018).
85 E. Aydin, T. G. Allen, M. de Bastiani, L. Xu, J. Ávila, M. Salvador, E. van Kerschaver, and S. de Wolf, Nat. Energy **5**, 851 (2020).
86 S. Turren-Cruz, A. Hagfeldt, and M. Saliba, Science **362**, 449 (2018).
87 C. C. Stoumpos, C. D. Malliakas, J. A. Peters, Z. Liu, M. Sebastian, J. Im, T. C. Chasapis, A. C. Wibowo, D. Y. Chung, A. J. Freeman, B. W. Wessels, and M. G. Kanatzidis, Cryst. Growth Des. **13**, 2722 (2013).
88 T. Malinauskas, D. Tomkute-Luksiene, R. Sens, M. Daskeviciene, R. Send, H. Wonneberger, V. Jankauskas, I. Bruder, and V. Getautis, ACS Appl. Mater. Interfaces **7**, 11107 (2015).
89 A. Abate, T. Leijtens, S. Pathak, J. Teuscher, R. Avolio, M. E. Errico, J. Kirkpatrik, J. M. Ball, P. Docampo, I. McPherson, and H. J. Snaith, Phys. Chem. Chem. Phys. **15**, 2572 (2013).
90 J. Y. Seo, H. S. Kim, S. Akin, M. Stojanovic, E. Simon, M. Fleischer, A. Hagfeldt, S. M. Zakeeruddin, and M. Grätzel, Energy Environ. Sci. **11**, 2985 (2018).
91 N. J. Jeon, H. Na, E. H. Jung, T. Y. Yang, Y. G. Lee, G. Kim, H. W. Shin, S. Il Seok, J. Lee, and J. Seo, Nat. Energy **3**, 682 (2018).
92 Q. Wang, C. Bi, and J. Huang, Nano Energy **15**, 275 (2015).
93 N. Y. Nia, M. Zendehdel, M. Abdi-Jalebi, L. A. Castriotta, F. U. Kosasih, E. Lamanna, M. M. Abolhasani, Z. Zheng, Z. Andaji-Garmaroudi, K. Asadi, G. Divitini, C. Ducati, R. H. Friend, and A. Di Carlo, Nano Energy **82**, 105685 (2021).
94 F. Cheng, R. He, S. Nie, C. Zhang, J. Yin, J. Li, N. Zheng, and B. Wu, J. Am. Chem. Soc. **143**, 5855 (2021).
95 H. Wang, P. Wang, Y. Sun, C. Gao, W. Miao, D. Li, Y. Yang, T. Wang, and D. Liu, Adv. Funct. Mater. **32**, 2201935 (2022).
96 M. Spalla, L. Perrin, E. Planes, M. Matheron, S. Berson, and L. Flandin, ACS Appl. Energy Mater. **3**, 3282 (2020).
97 P. Lin, W. Zhang, L. Tian, L. Jia, F. Wen, G. Duan, X. Zhou, S. Zhou, F. Zhang, Y. Jiang, T. Chen, F. Liu, S. Yang, and Y. Huang, ACS Appl. Energy Mater. **4**, 4408 (2021).
98 Z. Liu, L. Wang, C. Xu, X. Xie, and Y. Zhang, ACS Appl. Energy Mater. **4**, 10574 (2021).
99 J. You, L. Meng, T. B. Song, T. F. Guo, Y. M. Yang, W. H. Chang, Z. Hong, H. Chen, H. Zhou, Q. Chen, Y. Liu, N. de Marco, and Y. Yang, Nat. Nanotech. **11**, 75 (2016).
100 D. Chi, S. Huang, M. Zhang, S. Mu, Y. Zhao, Y. Chen, and J. You, Adv. Funct. Mater. **28**, 1804603 (2018).

101 L. Yang, F. Cai, Y. Yan, J. Li, D. Liu, A. J. Pearson, and T. Wang, Adv. Funct. Mater. **27**, 1702613 (2017).

102 X. Zhao, H. S. Kim, J. Y. Seo, and N. G. Park, ACS Appl. Mater. Interfaces **9**, 7148 (2017).

103 W. A. Dunlap-Shohl, T. Li, and D. B. Mitzi, ACS Appl. Energy Mater. **2**, 5083 (2019).

104 S. Thampy, B. Zhang, K. H. Hong, K. Cho, and J. W. P. Hsu, ACS Energy Lett. **5**, 1147 (2020).

105 C. Tian, A. Mei, S. Zhang, H. Tian, S. Liu, F. Qin, Y. Xiong, Y. Rong, Y. Hu, Y. Zhou, S. Xie, and H. Han, Nano Energy **53**, 160 (2018).

106 A. Mei, Y. Sheng, Y. Ming, Y. Hu, Y. Rong, W. Zhang, S. Luo, G. Na, C. Tian, X. Hou, Y. Xiong, Z. Zhang, S. Liu, S. Uchida, T. W. Kim, Y. Yuan, L. Zhang, Y. Zhou, and H. Han, Joule **4**, 2646 (2020).

107 F. H. Isikgor, F. Furlan, J. Liu, E. Ugur, M. K. Eswaran, A. S. Subbiah, E. Yengel, M. de Bastiani, G. T. Harrison, S. Zhumagali, C. T. Howells, E. Aydin, M. Wang, N. Gasparini, T. G. Allen, A. Rehman, E. van Kerschaver, D. Baran, I. McCulloch, T. D. Anthopoulos, U. Schwingenschlögl, F. Laquai, and S. de Wolf, Joule **5**, 1566 (2021).

108 Y. Li, B. Shi, Q. Xu, L. Yan, N. Ren, Y. Chen, W. Han, Q. Huang, Y. Zhao, and X. Zhang, Adv. Energy Mater. **11**, 2102046 (2021).

109 K. Sivula, Z. T. Ball, N. Watanabe, and J. M. J. Fréchet, Adv. Mater. **18**, 206 (2006).

110 C. Z. Li, H. L. Yip, and A. K. Y. Jen, J. Mater. Chem. **22**, 4161 (2012).

111 S. H. Li, Z. Xing, B. S. Wu, Z. C. Chen, Y. R. Yao, H. R. Tian, M. F. Li, D. Q. Yun, L. L. Deng, S. Y. Xie, R. B. Huang, and L. S. Zheng, ACS Appl. Mater. Interfaces **12**, 20733 (2020).

112 D. B. Amabilino, *Supramolecular Chemistry at Surfaces* (The Royal Society of Chemistry, London, 2016).

113 R. Cheacharoen, N. Rolston, D. Harwood, K. A. Bush, R. H. Dauskardt, and M. D. McGehee, Energy Environ. Sci. **11**, 144 (2018).

114 C. Tian, G. Betancourt-Solis, Z. Nan, K. Liu, K. Lin, J. Lu, L. Xie, L. Echegoyen, and Z. Wei, Sci. Bull. **66**, 339 (2021).

115 Q. Emery, M. Remec, G. Paramasivam, S. Janke, J. Dagar, C. Ulbrich, R. Schlatmann, B. Stannowski, E. Unger, and M. Khenkin, ACS Appl. Mater. Interfaces **14**, 5159 (2022).

116 Y. H. Lin, N. Sakai, P. Da, J. Wu, H. C. Sansom, A. J. Ramadan, S. Mahesh, J. Liu, R. D. J. Oliver, J. Lim, L. Aspitarte, K. Sharma, P. K. Madhu, A. B. Morales-Vilches, P. K. Nayak, S. Bai, F. Gao, C. R. M. Grovenor, M. B. Johnston, J. G. Labram, J. R. Durrant, J. M. Ball, B. Wenger, B. Stannowski, and H. J. Snaith, Science **369**, 96 (2020).

117 T. Matsui, T. Yamamoto, T. Nishihara, R. Morisawa, T. Yokoyama, T. Sekiguchi, and T. Negami, Adv. Mater. **31**, 1806823 (2019).

118 A. K. Baranwal, S. Kanaya, T. A. N. Peiris, G. Mizuta, T. Nishina, H. Kanda, T. Miyasaka, H. Segawa, and S. Ito, ChemSusChem **9**, 2604 (2016).

119 I. T. S. Heikkinen, G. Koutsourakis, S. Virtanen, M. Yli-Koski, S. Wood, V. Vähänissi, E. Salmi, F. A. Castro, and H. Savin, J. Vacuum Sci. Tech. A **38**, 022401 (2020).

120 B. Phua, X. Shen, P. C. Hsiao, C. Kong, A. Stokes, and A. Lennon, Sol. Energy Mater. Sol. Cells **215**, 110638 (2020).

121 J. Karas, L. Michaelson, K. Munoz, M. Jobayer Hossain, E. Schneller, K. O. Davis, S. Bowden, and A. Augusto, Prog. Photovolt.-Res. Appl. **28**, 1175 (2020).

122 D. Chen, M. Vaqueiro Contreras, A. Ciesla, P. Hamer, B. Hallam, M. Abbott, and C. Chan, Prog. Photovolt.-Res. Appl. **29**, 1180 (2021).

123 K. R. McIntosh, and X. Dai, Phys. Status Solidi A **208**, 1931 (2011).

124 A. Thomson, M. Gardner, K. McIntosh, A. Shalav, and J. Bullock, J. Appl. Phys. **115**, 114505 (2014).

125 N. Kyranaki, A. Smith, K. Yendall, D. A. Hutt, D. C. Whalley, R. Gottschalg, and T. R. Betts, Prog. Photovolt. **30**, 1061 (2022).

126 C. Yi, J. Luo, S. Meloni, A. Boziki, N. Ashari-Astani, C. Grätzel, S. M. Zakeeruddin, U. Röthlisberger, and M. Grätzel, Energy Environ. Sci. **9**, 656 (2016).

127 X. Wang, Y. Chen, T. Zhang, X. Wang, Y. Wang, M. Kan, Y. Miao, H. Chen, X. Liu, X. Wang, J. Shi, L. Zhang, and Y. Zhao, ACS Energy Lett. **6**, 2735 (2021).

128 J. Xu, C. C. Boyd, Z. J. Yu, A. F. Palmstrom, D. J. Witter, B. W. Larson, R. M. France, J. Werner, S. P. Harvey, E. J. Wolf, W. Weigand, S. Manzoor, M. F. A. M. van Hest, J. J. Berry, J. M. Luther, Z. C. Holman, and M. D. McGehee, Science **367**, 1097 (2020).

129 L. Wang, G. Wang, Z. Yan, J. Qiu, C. Jia, W. Zhang, C. Zhen, C. Xu, K. Tai, X. Jiang, and S. Yang, Sol. RRL **4**, 2000098 (2020).

130 D. Kim, H. J. Jung, I. J. Park, B. W. Larson, S. P. Dunfield, C. Xiao, J. Kim, J. Tong, P. Boonmongkolras, S. G. Ji, F. Zhang, S. R. Pae, M. Kim, S. B. Kang, V. Dravid, J. J. Berry, J. Y. Kim, K. Zhu, D. H. Kim, and B. Shin, Science **368**, 155 (2020).

131 H. Tsai, W. Nie, J. C. Blancon, C. C. Stoumpos, R. Asadpour, B. Harutyunyan, A. J. Neukirch, R. Verduzco, J. J. Crochet, S. Tretiak, L. Pedesseau, J. Even, M. A. Alam, G. Gupta, J. Lou, P. M. Ajayan, M. J. Bedzyk, M. G. Kanatzidis, and A. D. Mohite, Nature **536**, 312 (2016).

132 Y. Lin, Y. Bai, Y. Fang, Q. Wang, Y. Deng, and J. Huang, ACS Energy Lett. **2**, 1571 (2017).

133 Y. Bai, S. Xiao, C. Hu, T. Zhang, X. Meng, H. Lin, Y. Yang, and S. Yang, Adv. Energy Mater. **7**, 1701038 (2017).

134 L. Su, Y. Xiao, G. Han, L. Lu, H. Li, and M. Zhu, J. Power Sources **426**, 11 (2019).

135 A. A. Sutanto, R. Szostak, N. Drigo, V. I. E. Queloz, P. E. Marchezi, J. C. Germino, H. C. N. Tolentino, M. K. Nazeeruddin, A. F. Nogueira, and G. Grancini, Nano Lett. **20**, 3992 (2020).

136 X. Guo, Y. Gao, Q. Wei, K. Ho Ngai, M. Qin, X. Lu, G. Xing, T. Shi, W. Xie, J. Xu, and M. Long, Sol. RRL **5**, 2100555 (2021).

137 H. Yu, Y. Xie, J. Zhang, J. Duan, X. Chen, Y. Liang, K. Wang, and L. Xu, Adv. Sci. **8**, 2004510 (2021).

138 J. W. Lee, Z. Dai, T. H. Han, C. Choi, S. Y. Chang, S. J. Lee, N. de Marco, H. Zhao, P. Sun, Y. Huang, and Y. Yang, Nat. Commun. **9**, 3021 (2018).

139 C. Zhang, S. Wu, L. Tao, G. M. Arumugam, C. Liu, Z. Wang, S. Zhu, Y. Yang, J. Lin, X. Liu, R. E. I. Schropp, and Y. Mai, Adv. Energy Mater. **10**, 2002004 (2020).

140 C. F. J. Lau, Z. Wang, N. Sakai, J. Zheng, C. H. Liao, M. Green, S. Huang, H. J. Snaith, and A. Ho-Baillie, Adv. Energy Mater. **9**, 1901685 (2019).

141 W. Li, B. Zhu, M. U. Rothmann, A. Liu, W. Chen, Y. Y. Choo, N. Pai, W. Mao, T. Zhang, Q. Bao, X. Wen, U. Bach, J. Etheridge, and Y. B. Cheng, Sci. China Mater. **64**, 2655 (2021).

142 S. Zhumagali, F. H. Isikgor, P. Maity, J. Yin, E. Ugur, M. de Bastiani, A. S. Subbiah, A. J. Mirabelli, R. Azmi, G. T. Harrison, J. Troughton, E. Aydin, J. Liu, T. Allen, A. Rehman, D. Baran, O. F. Mohammed, and S. de Wolf, Adv. Energy Mater. **11**, 2101662 (2021).

143 K. Suwa, L. Cojocaru, K. Wienands, C. Hofmann, P. S. C. Schulze, A. J. Bett, K. Winkler, J. C. Goldschmidt, S. W. Glunz, and H. Nishide, ACS Appl. Mater. Interfaces **12**, 6496 (2020).

144 M. Neophytou, M. de Bastiani, N. Gasparini, E. Aydin, E. Ugur, A. Seitkhan, F. Moruzzi, Y. Choaie, A. J. Ramadan, J. R. Troughton, R. Hallani, A. Savva, L. Tsetseris, S. Inal, D. Baran, F. Laquai, T. D. Anthopoulos, H. J. Snaith, S. de Wolf, and I. McCulloch, ACS Appl. Energy Mater. **2**, 8090 (2019).

145 K. A. Bush, C. D. Bailie, Y. Chen, A. R. Bowring, W. Wang, W. Ma, T. Leijtens, F. Moghadam, and M. D. McGehee, Adv. Mater. **28**, 3937 (2016).

146 K. A. Bush, A. F. Palmstrom, Z. J. Yu, M. Boccard, R. Cheacharoen, J. P. Mailoa, D. P. McMeekin, R. L. Z. Hoye, C. D. Bailie, T. Leijtens, I. M. Peters, M. C. Minichetti, N. Rolston, R. Prasanna, S. Sofia, D. Harwood, W. Ma, F. Moghadam, H. J. Snaith, T. Buonassisi, Z. C. Holman, S. F. Bent, and M. D. McGehee, Nat. Energy **2**, 17009 (2017).

147 J. Zheng, H. Mehrvarz, C. Liao, J. Bing, X. Cui, Y. Li, V. R. Gonçales, C. F. J. Lau, D. S. Lee, Y. Li, M. Zhang, J. Kim, Y. Cho, L. G. Caro, S. Tang, C. Chen, S. Huang, and A. W. Y. Ho-Baillie, ACS

Energy Lett. **4**, 2623 (2019).
148 K. Choi, J. Lee, H. Choi, G. W. Kim, H. I. Kim, and T. Park, Energy Environ. Sci. **13**, 5059 (2020).
149 G. S. Han, J. S. Yoo, F. Yu, M. L. Duff, B. K. Kang, and J. K. Lee, J. Mater. Chem. A **5**, 14733 (2017).
150 X. Sun, T. J. Silverman, Z. Zhou, M. R. Khan, P. Bermel, and M. A. Alam, IEEE J. Photovolt. **7**, 566 (2017).
151 S. Lin, L. Ai, J. Zhang, T. Bu, H. Li, F. Huang, J. Zhang, Y. Lu, and W. Song, Sol. Energy Mater. Sol. Cells **203**, 110135 (2019).
152 J. Qian, A. F. Thomson, Y. Wu, K. J. Weber, and A. W. Blakers, ACS Appl. Energy Mater. **1**, 3025 (2018).
153 B. Li, J. Yu, P. Wang, J. He, R. Su, L. Wang, J. Li, W. Wu, X. Cui, T. Chen, and Y. Huang, Sol. Energy **225**, 634 (2021).
154 P. Mariani, L. Najafi, G. Bianca, M. I. Zappia, L. Gabatel, A. Agresti, S. Pescetelli, A. Di Carlo, S. Bellani, and F. Bonaccorso, ACS Appl. Mater. Interfaces **13**, 22368 (2021).
155 D. Bogachuk, K. Saddedine, D. Martineau, S. Narbey, A. Verma, P. Gebhardt, J. P. Herterich, N. Glissmann, S. Zouhair, J. Markert, I. E. Gould, M. D. McGehee, U. Würfel, A. Hinsch, and L. Wagner, Sol. RRL **6**, 2100527 (2022).